COLLISIONLESS DIFFUSION IN TWO-FREQUENCY ELECTRON CYCLOTRON RESONANCE HEATING

by

J. E. Howard, A. J. Lichtenberg,

M. A. Lieberman and R. H. Cohen

Memorandum No. UCB/ERL M83/65

27 April 1983

ELECTRONICS RESEARCH LABORATORY

College of Engineering
University of California, Berkeley
94720

COLLISIONLESS DIFFUSION IN TWO-FREQUENCY ELECTRON CYCLOTRON RESONANCE HEATING

J. E. Howard, A. J. Lichtenberg, and M. A. Lieberman

University of California, Berkeley

R. H. Cohen

Lawrence Livermore National Laboratory

ABSTRACT

Two-frequency electron cyclotron resonance heating (ECRH) is modelled by a four-dimensional mapping derived from the nonrelativistic single particle equations of motion. The model includes changes in parallel energy due to the spatially separate resonance zones, not given by previous two-dimensional models. Fixed points are located and their linear stability limits determined. Resonances in action space are calculated along with their widths and used to obtain the adiabatic barrier to heating. Quasilinear diffusion coefficients are derived for the stochastic regime and found to agree well with numerical calculations. The intrinsic diffusion in parallel energy leads to axial losses in a magnetic trap which can rival those induced by collisions. An analytic model for this process gives a loss rate in good agreement with a numerical simulation. Arnold diffusion along a resonance layer is also treated theoretically, yielding diffusion coefficients in reasonable agreement with numerical values. A more complete four-dimensional mapping is derived and used to modify the results from the simpler mapping to determine the quasilinear diffusion rate into the loss cone and the rate of Arnold diffusion through the adiabatic barrier for practical ECRH experiments.

I. Introduction

Electron cyclotron resonance heating (ECRH) is a well-established method of heating electrons to high temperatures[1,2] and an important component of several proposed fusion devices.[3,4] For these reasons ECRH has been widely used in plasma experiments and has motivated a number of theoretical studies.[5,6] Recent experiments[7] using two or more sources with closely spaced frequencies show a significant increase in electron energy density over the single frequency result for the same total input power.

Several theoretical and numerical studies have been carried out to explain the observed enhancement. Monte Carlo simulations by Samec et al.[8] and by Rognlien[9] show a significant increase in the limiting particle energy E_B and the diffusion coefficient near E_B when two or more frequencies are employed. The two-frequency diffusion coefficient was maximally enhanced when the frequency separation was an odd multiple of the bounce frequency,

$$\Delta\omega = (2m-1)\omega_b, \quad m = 1,2,3,... \tag{1}$$

in general agreement with the experiment. Howard et al.,[10,11] using two-dimensional mapping models, predict an approximate doubling of the maximum energy E_B over the single frequency limit when (1) is satisfied.

In this paper we treat two-frequency ECRH more completely by means of a four-dimensional mapping that includes perturbations in the parallel energy as well as in the perpendicular energy. This generalization allows us to examine the island overlap criterion in the full phase space and to study the consequences of higher dimensionality, such as Arnold diffusion,[12] on the wave-particle interaction.

Early ECRH theories assumed that successive passes through each resonance zone were uncorrelated, implying quasilinear diffusive heating.[6] On the other hand, a Hamiltonian perturbative calculation[13] predicted ordered motion in the absence of collisions. These opposing viewpoints were resolved by a more complete analysis,[5] which showed that either ordered or stochastic motion could occur, depending on the heating parameters and the particle energy. A single-frequency ECRH map was derived assuming narrow heating zones near the orbital turning points, and used to interpret an ECRH experiment.[2] The ECRH map was also related to simpler systems such as the Fermi map and the Chirikov "standard map."[12]

In general, the two-dimensional phase space of an electron being heated by a cyclotron wave in a magnetic mirror is divided into three regions; a stochastic region at low energies; a primarily regular (adiabatic) region at high energies; and an intermediate region in which regular islands are embedded in a stochastic sea. The lowest phase-spanning Kolmogorov-Arnold-Moser (KAM) curve acts as a barrier to heating from below. The diffusion rate in the intermediate region drops off sharply from an approximately quasilinear value at lower energies to zero at the KAM barrier.

Previous ECRH theory was extended to two-frequency heating by Howard et al., first by employing the Fermi mapping as an analog to particle heating in a magnetic trap,[10] and then by deriving a two-dimensional two-frequency ECRH mapping.[11] Both treatments showed that the stochastic heating limit could be significantly enhanced using two frequencies by interspersing the corresponding sets of phase space islands. The frequency condition (1) was shown to arise naturally in both problems as a consequence of interleaving the second set of islands midway between the first set of islands in the region near the single frequency barrier.

Experimental evidence for the existence of such adiabatic barriers is scant; two high-power pulsed ECRH experiments, in which collisional effects are unimportant, appear to show a heating limit consistent with theory.[2,11] Adiabatic barriers calculated for low field, large volume, long pulse experiments are usually well below observed particle energies.[11] However, collisional effects and second harmonic heating may have played a crucial role in these experiments. The recent symmetric tandem mirror (STM) experiments using long-pulse power divided among up to four closely-spaced frequencies show an increase in energy density over the single frequency level, in general agreement with numerical simulations and theoretical predictions based on the interspersal of resonances in phase space. The electron rings in STM are produced by second-harmonic heating of a bulk plasma heated at the fundamental. The picture that emerges from the theoretical and computational work summarized above is that using multiple frequencies raises the stochastic heating limit for the fundamental, thereby enhancing the efficiency of fueling for second-harmonic heating, the diffusion coefficient for the latter being an increasing function of perpendicular energy. Thus, the hot electron energy density is increased.

The four-dimensional aspects of two-frequency heating treated in this paper are of interest from the standpoint of nonlinear dynamics, as well as for their physical applications. In Sec. II a simplified version of the four-dimensional ECRH mapping is derived and related to previous two-dimensional mappings. In particular, the velocity dependences of $\Delta E_{\perp}$ and $\Delta E_{\parallel}$ are replaced by constants. This assumption retains much of the essential physics, while enabling us to study four-dimensional effects with relative ease. Linear stability analysis of the physically important phase space islands entails calculating the eigenvalues of a four-by-four symplectic matrix.[14] This is done analytically in Sec. III for a subclass of fixed points and numerically for the general case. The adiabatic (KAM) barrier to heating is usually found from a resonance overlap criterion such as the two-thirds rule.[12] However, for our four-dimensional mapping the resonances are staggered in phase, so that the usual overlap criteria do not apply. This problem is analyzed in Sec. IV, yielding an adiabatic barrier in action space in excellent agreement with numerical solutions of the mapping equations.

Another important consequence of the higher dimensionality of the phase space is Arnold diffusion,[12] which can move particles along resonance layers as well as across them. "Thick layer" Arnold diffusion, which may be regarded a ordinary quasilinear diffusion, occurs in the (mostly) stochastic region below the adiabatic barrier. This diffusion is an intrinsic process driven by the dynamics rather than by an extrinsic source such as particle collisions. The resulting diffusion in parallel energy drives an axial loss process in a magnetic trap at a rate which can exceed that due to collisional loss-cone diffusion. "Thin layer" Arnold diffusion is a subtle effect which causes particles to diffuse along the relatively thin resonance layers above the adiabatic barrier. A potentially important consequence is that particles may leak through the adiabatic barriers and be carried along resonances to arbitrarily high energies. The diffusion rates for both thick and thin layer diffusion are derived in Sec. V. Section VI describes a mirror loss-cone model which gives the axial loss rate and the average energy of lost particles due to thick layer diffusion. The results are shown to compare well with a numerical simulation.

Although all qualitative features of two frequency ECRH dynamics are given by the simplified four dimensional mapping of Sec. II, quantitative values of energy limits and diffusion rates in real experiments cannot be predicted. The energy dependences of the heating coefficients (powers of perpendicular energy multiplied by Airy functions) are reintroduced into the mapping in Sec. VII. The various requirements of a physical ECRH configuration on the mapping are discussed, and predictions of heating limits for experimental devices are given. The roles of the Airy functions in limiting the allowable frequency separation and in setting barriers to diffusion are discussed. In Sec. VIII the diffusion results of Secs. V and VI are applied to the more realistic ECRH mapping to determine the rate of diffusion into the loss cone and the rate of diffusion to energies above the adiabatic heating barrier. This intrinsic diffusion is compared with the extrinsic diffusion due to collisions for the STM experiments.

II. Mapping Model

A. Derivation of Four-Dimensional Mapping

Consider a trapped particle gyrating in a parabolic magnetic well

$$B = B_0 \, (1 + z^2/L^2) \tag{2}$$

with two closely-spaced resonance zones near each turning point, as depicted in Fig. 1. Assuming that the orbit initially penetrates the inner resonance zone, it will tend to turn there, since for $k_{\|} v_{\|} << c$ the wave changes $v_\perp$, but not $v_{\|}$. It is convenient to imagine a surface of section just inside the inner resonance zone at z_1, as shown in Fig. 1. If all four resonances on one side of the midplane are well-merged, we may lump the two kicks at z_1 together to obtain

$$\Delta E_{\perp_1} = A_1 \sin(\theta - \omega_1 t) \tag{3}$$

where

$$\theta = \int^t \omega_{ce} \, dt \tag{4}$$

is the gyrophase and A_1 is a function of $v_\perp$ and $v_{\|}$ involving the Airy function. Similarly, lumping the two resonances at z_2 together gives

$$\Delta E_{\perp_2} = A_2 \sin(\theta - \omega_2 t). \tag{5}$$

As usual, we assume that the parallel energy is locally unaffected by the wave; however, there is an indirect change in $E_{\parallel}$ at z_1 due to the kick in $E_{\perp}$ at z_2. Using the conservation of magnetic moment $v_{\perp}^2/B$ and total energy between resonance zones, we readily find expressions for the net change at z_1 after traversing n resonance pairs in an arbitrary concave well,

$$\Delta E_{\perp} = \sum_{k=1}^{n} \frac{R_1}{R_k} \Delta E_{\perp_k} \tag{6}$$

$$\Delta E_{\parallel} = \sum_{k=1}^{n} (1 - \frac{R_1}{R_k}) \Delta E_{\perp_k}$$

where $\Delta E_{\perp_k}$ is the kick due to the k^{th} resonance pair and $R_k = B_k/B_0$ is the local mirror ratio. For two resonance frequencies, Eqs. (3) and (6) give

$$\Delta E_{\perp} = A_1 \sin\psi + \frac{R_1}{R_2} A_2 \sin(\psi + \xi) \tag{7a}$$

$$\Delta E_{\parallel} = \frac{\delta\omega}{\omega_1} \frac{R_1}{R_2} A_2 \sin(\psi + \xi), \tag{7b}$$

where $\delta\omega/\omega_1 = R_2/R_1 - 1$, and

$$\psi = \theta - \omega_1 t \tag{8}$$

$$\xi = -t\, \delta\omega.$$

The phase slip between turning points in a parabolic well may be written

$$\Delta\psi = -\frac{\pi}{2} R_1^{1/2} \omega_1 L \frac{(\rho E_{\perp} - E_{\parallel})}{E_{\perp}^{3/2}}, \tag{9}$$

where $\rho = 1 - 1/R_1$. The half-bounce time in a parabolic well is

$$\frac{1}{2} \tau_b = \pi L (R_1/E_{\perp})^{1/2} \tag{10}$$

so that the change in the bounce phase is

$$\Delta\xi = -\pi L\, \delta\omega\, (R_1/E_{\perp})^{1/2}. \tag{11}$$

Equations (7), (9) and (11) constitute a four dimensional mapping which approximates the heating process for a single pass through both resonance pairs. However, since A_1 and A_2 are functions of $E_{\perp}$ and $E_{\parallel}$, this mapping is not area-preserving and therefore does not realistically model the motion over many iterations. This deficiency is easily remedied by the addition of small correction terms to the phase advance equations (9) and (11), as described in Sec. VII. Here we treat A_1 and A_2 as constants, which greatly simplifies the analysis and numerical calculations, while retaining the essential four dimensional effects of multifrequency heating. In this approximation the variables $E_\perp$, ψ, $(\omega/\delta\omega)E_\parallel$, ξ are a canonical set, yielding a symplectic (and therefore area-preserving) mapping.

It is useful to modify this mapping in such a way that one of the phases is relatively slowly varying. This may be done by introducing the slow phase

$$\chi = \xi - \sigma\psi \tag{12}$$

with

$$\sigma = \frac{2}{\rho}\frac{\delta\omega}{\omega}, \tag{13}$$

while retaining ψ as the fast phase. Making the necessary canonical transformations, we obtain the new action variables

$$P = \frac{1}{N A_1}\left(E_\perp + \frac{2}{\rho} E_\parallel\right) \tag{14}$$

$$J = \frac{1}{N A_1}\left(\frac{\omega_1}{\delta\omega}\right) E_\parallel \tag{15}$$

where we have introduced the normalization factor

$$N = (1 + \lambda^2 \epsilon^2)^{1/2} \tag{16}$$

with

$$\lambda = 1 + \sigma \tag{17}$$

and

$$\epsilon = \frac{R_1}{R_2}\frac{A_2}{A_1}. \tag{18}$$

After these transformations we obtain the symplectic mapping

$$P' = P + \frac{1}{N}\left[\sin\psi + \epsilon\lambda \sin(\lambda\psi + \chi)\right] \tag{19a}$$

$$J' = J + \frac{\epsilon}{N} \sin (\lambda\psi + \chi) \tag{19b}$$

$$\psi' = \psi - \frac{M}{u'} + \frac{\sigma M J'}{2 (u')^3} \tag{19c}$$

$$\chi' = \chi - \frac{\sigma^2 M J'}{2 (u')^3} \tag{19d}$$

where

$$M = \frac{\pi \omega_1 L \rho R_1^{1/2}}{(2A_1 N)^{1/2}} \tag{20}$$

and

$$u^2 = P - \sigma J \tag{21}$$

is proportional to $E_\perp$. The angle χ is slowly varying for $\sigma << 1$. Note that updated values of u and J are used in the phase advance equations. The dimensionless parameter M is related to the total phase slip between turning points, analogous to the parameter M employed in previous treatments of the single frequency ECRH map and the two-frequency Fermi mapping.[10] The normalization N is introduced to approximately fix the total power in the two waves as ϵ is varied. The complete four-dimensional mapping (19) may be derived from the generating function

$$S(P',J',\psi,\chi) = P'\psi + J'\chi + \frac{1}{N} [\cos\psi + \epsilon \cos(\lambda\psi + \chi)] - \frac{M}{u'} (2P' - \sigma J'). \tag{22}$$

The mapping in the form (19) will be used in our calculations of Arnold diffusion. However, for numerical calculation of fixed points, linear stability, resonances and adiabatic barriers it is convenient to restrict λ to rational values $\lambda = r/s$, with $r = s+1$ so that $\sigma = 1/s$. Introducing the new pair of conjugate variables

$$I = s\,P \tag{23}$$
$$\phi = \psi/s$$

then gives a mapping periodic in ϕ,

$$I' = I + \frac{s}{N} [\sin (s\phi) + \epsilon\lambda \sin(r\phi + \chi)]$$

$$J' = J + \frac{\epsilon}{N} \sin(r\phi + \chi) \tag{24}$$

$$\phi' = \phi - \sigma \frac{M}{u'} + \frac{\sigma^2 M J'}{2(u')^3}$$

$$\chi' = \chi - \frac{\sigma^2 M J'}{2(u')^3}.$$

B. Reduction to two-dimensional mapping

The four-dimensional mapping may be compared with the two-dimensional two-frequency Fermi mapping[10] by expanding Eqs. (19c,d) in powers of $\sigma << 1$;

$$\psi' = \psi - \frac{M}{(P')^{1/2}} + \frac{3 M \sigma^2 (J')^2}{8(P')^{5/2}} + \cdots \tag{25a}$$

$$\chi' = \chi - \frac{\sigma^2 M J'}{2(P')^{3/2}} + \cdots \tag{25b}$$

Thus, to order σ , χ = constant; Eqs. (19a) and (25a) then constitute a two dimensional mapping with χ and J as parameters. Taking $\chi = 0$ for convenience and reintroducing ϕ we have

$$P' = P + \frac{1}{N} (\sin s\phi + \hat{\epsilon} \sin r\phi) \tag{26}$$

$$\phi' = \phi - \frac{2\pi \hat{M}}{(P')^{1/2}}$$

where $\hat{\epsilon} \equiv \lambda \epsilon$ and $\hat{M} \equiv \sigma M/2\pi$.

Except for the power of the action occuring in the phase advance, this mapping is identical to the two-frequency Fermi mapping studied previously[10]. Consequently, the general conclusions reached in Ref. 10 apply to the present problem whenever the reduced mapping (26) is valid. In particular, we can employ secular perturbation theory to expand about the two-dimensional resonances to obtain the two-thirds rule for the overlap of neighboring islands,

$$\Delta P_1 + \Delta P_2 \geqslant \frac{2}{3} \, | P_1 - P_2 | \tag{27}$$

where ΔP_1 and ΔP_2 are the resonance half- widths and P_1 and P_2 are the neighboring resonance values. For single frequency heating with $\epsilon = 0$, Eq. (27) reduces to the overlap criterion for the standard map, namely that the Chirikov parameter

$$K \; = \; \Delta P \, \frac{\partial (s\phi)}{\partial P} \; = \; \frac{\hat{M}}{2P^{3/2}} \geqslant 1. \tag{28}$$

Thus, the barrier to heating from below is approximately

$$P_B \; = \; (\frac{1}{2}\hat{M})^{2/3}. \tag{29}$$

When the heating power is divided between two frequencies ($\hat{\epsilon} \neq 0$) the KAM barrier exceeds the single frequency value (29) by an amount that is maximized when the s-fold resonances given by $s\Delta\phi \; = 2\pi n_s$ are interspersed midway between the r-fold resonances $r\Delta\phi \; = \; 2\pi n_r$ at the stability boundary. For $\hat{\epsilon} \neq 0$, the factor K/N is proportional to the square of the ratio of the resonance separation $(P_1 - P_2)$ to the resonance width for the s-fold resonances, while $\lambda \hat{\epsilon} K/N$ has the same interpretation for the r-fold resonances.

The reduced mapping (26) is a fair representation of the full mapping (24) provided that three conditions are met. First, the third term in (25a) must be small compared with the second, which is true if $(\sigma J)^2 << 3P^2$. Secondly, the cumulative effect of the neglected terms over some specified time n must be small, i. e.

$$\frac{3\hat{M}\sigma^2 J^2}{P^{5/2}} << \frac{1}{n} \tag{30}$$

$$\frac{\sigma^2 \hat{M} J}{2P^{3/2}} << \frac{1}{n}. \tag{31}$$

The second of these is the most important, since $\Delta\psi$ can be an arbitrary function of P' and still maintain area-preservation, it may be written

$$\sigma J << \frac{1}{\sigma n} \left(\frac{P}{P_B} \right)^{3/2}, \tag{32}$$

where we have used (29). Thus, for $P \approx P_B$ the time over which the mapping remains two-dimensional is proportional to $\sigma^{-2} J^{-1}$.

III. Fixed Points and Linear Stability

A. Location of Fixed Points

To locate the fixed points in ϕ and χ we set $\Delta I = \Delta J = 0$ in (24), which gives the simultaneous equations

$$\sin s\phi + \epsilon\lambda \sin(r\phi+\chi) = 0 \tag{33a}$$

$$\sin(r\phi+\chi) = 0. \tag{33b}$$

Combining (33a) and (33b), we obtain $\sin s\phi = 0$, so that

$$\phi_k = k\pi/s, \quad k = 0, \pm 1, \pm 2, \cdots . \tag{34}$$

Equation (33b) then implies

$$\chi_k = -\phi_k, \ \pi - \phi_k. \tag{35}$$

so that the period-one fixed points lie along diagonal lines in the $\phi - \chi$ plane.

To locate the fixed points in I and J, we set

$$\Delta\phi = -2\pi n, \quad n = 0, \pm 1, \cdots \tag{36}$$

$$\Delta\chi = -2\pi m, \quad m = 0, \pm 1, \cdots$$

or

$$\frac{\sigma M}{u} - \frac{\sigma^2 MJ}{2u^3} = 2\pi n \tag{37a}$$

$$\frac{\sigma^2 MJ}{2u^3} = 2\pi m. \tag{37b}$$

Combining (37a) and (37b) gives the fixed points in velocity,

$$u_{nm} = \frac{\sigma M}{2\pi(n+m)}. \tag{38}$$

Using this result in (37) then gives

$$I_{nm} = \frac{(n+3m)I_0}{(n+m)^3}, \tag{39}$$

$$J_{nm} = \frac{2m\ I_0}{(n+m)^3}, \tag{40}$$

where

$$I_0 \equiv \sigma(\frac{M}{2\pi})^2. \tag{41}$$

Recalling that I and J may be negative, we see that all n and m are allowed, the only restriction being $n+m > 0$ to keep u, and therefore $v_\perp$, positive.

For $m = 0$, $J = 0$ and therefore

$$I_{n0} = I_0/n^2. \tag{42}$$

Dividing (39) by (40) we obtain

$$I_{nm} = J_{nm} + (\frac{m+n}{2m})J_{nm}$$

$$= J_{nm} + \frac{I_0}{(n+m)^2}$$

or

$$I_{nm} = I_{n+m,0} + J_{nm} \quad . \tag{43}$$

Thus, the fixed points of I and J lie along straight lines of slope unity, with $n+m$ = constant along each line, as depicted in Fig. 2.

Figures 3 and 4 show two-dimensional projections onto the $I-\phi$ plane for $\sigma = 1/4$, $M = 500$ and amplitude ratios $\epsilon = 0.05$ and 1.0. These surfaces of section were produced by scanning along a number of initial conditions in I, with $J_0 = 0$ and $(\phi_0,\chi_0) = (45°,135°)$. For these parameters we find stable "common" fixed points at $I_{0n} = 1583/n^2$ when $\epsilon = 0.05$, but which have evidently destabilized at $\epsilon = 1.0$. The reasons for the above choice of (ϕ_0,χ_0) and the instability at larger ϵ will be given in the next section.

B. Linear Stability

It is helpful in interpreting the various two-dimensional projections of (24), such as Figs. 3 and 4, to understand the local stability properties of the fixed points of the full four-dimensional map. This entails finding the eigenvalues of a 4x4 symplectic matrix, a problem considered by MacKay[14]. In this section we summarize the dependence of the linear stability of the period-one fixed points on M, σ, and ϵ. The detailed calculations are given in Appendix A.

The stability properties may be classified according to whether $J = 0$ or $J \neq 0$. We have applied the method of MacKay to the relatively tractable case $J = 0$, obtaining simple expressions for the stability boundaries. The more complicated case $J \neq 0$ has been studied numerically, and seems to result in less complicated stability limits, even though there are many more terms to be considered in the stability matrix. We have studied linear stability at three levels; first, by direct iteration of the mapping equations (24); second, by numerical computation of the eigenvalues; and third, analytically. We proceed by choosing a particular fixed point $(I_{mn}, J_{mn}, \phi_k, \chi_k)$. Next we fix M and observe the effects of increasing amplitude ratio ϵ. A preliminary numerical search shows that only a few combinations of (I,J,ϕ,χ) need be considered. First, all $J = 0$ cases are basically alike (for all n) and all $J \neq 0$ cases seem to be similar. In all cases only four combinations of (ϕ_k, χ_k) are independent, owing to the invariance of the mapping to the translation $\phi \rightarrow \phi + 2\pi\sigma, \chi \rightarrow \chi - 2\pi\sigma$. The two basic patterns in (ϕ,χ) for the "normal case" $\epsilon << 1$, $M >> 1$ are illustrated in Fig. 5 for $\sigma = 1/4$, $J = 0$, and $J \neq 0$, with the fixed points marked according to the observed stability. Thus, there are only four distinct combinations of (ϕ,χ) with only one of these stable. For $J = 0$ the only stable fixed point has $(\phi,\chi) = (45°,135°)$ when $\epsilon << 1$ (Fig. 3), while for $J \neq 0$ it is $(0°,180°)$.

As we have already seen in Fig. 4, the $J = 0$, $(45°,135°)$ fixed point goes unstable with increasing ϵ. The stability boundary in the $\epsilon - M$ plane is shown in Fig. 6 for $\sigma = 1/4$. Above a critical value, M_2, stability is lost when $\epsilon \geqslant 4/9$; for $M_1 > M > M_2$, the motion is stable to the right of the curve; for $M > M_2$, the motion is never stable. For $4/9 > \epsilon > 1$ there are no stable fixed points. When $\epsilon \geqslant 1$, however, the $(0°,180°)$ fixed point is stable to the left of the upper curve when $M_3 > M > M_4$, as shown in the right hand part of Fig. 6. Equations for the $J = 0$ stability boundaries and the limiting values M_1,M_2,M_3, and M_4 are given in Appendix A. We have also investigated the stability of the $J \neq 0$ fixed points by numerical calculation of the eigenvalues of the stability matrix. The results for the $(m,n) = (1,1)$, $(\phi,\chi) = (0°,180°)$, fixed point are shown in Fig. 7, which is characteristic of all cases investigated so far. Above a critical value, M_6, the motion is stable for $\epsilon > 1$; for $M_5 > M > M_6$ there is again a stability window; for $M > M_6$ the motion is never stable. In this case, the $(45°,135°)$ fixed point is always unstable, and no transitions occur at $\epsilon = 4/9$.

IV. Resonance Effects

A. Resonance Curves

From the mapping (24) the principal resonances are

$$s\,\Delta\phi = -2\pi n_s, \quad n_s = 0, \pm 1, \pm 2, \ldots \tag{44}$$

$$r\,\Delta\phi + \Delta\chi = -2\pi n_r, \quad n_r = 0, \pm 1, \pm 2, \cdots ,$$

corresponding to $\epsilon \to 0$ and ∞, respectively. Substituting expressions for $\Delta\phi$ and $\Delta\chi$ from (24) and solving for J, we obtain implicit equations for the resonance curves in the $I - J$ plane;

$$J_s = \frac{2u^2}{\sigma}\left(1 - \frac{u}{u_{s0}}\right) \tag{45}$$

$$J_r = \frac{2\lambda u^2}{\sigma}\left(1 - \frac{u}{u_{r0}}\right),$$

where

$$u_{s0} \equiv \frac{M}{2\pi n_s}, \quad u_{r0} = \frac{\lambda M}{2\pi n_r} .$$

Plots of I vs. J may be generated by treating u as a running parameter, with

$$I = J + u^2/\sigma. \tag{46}$$

Figure 8 shows a set of resonance curves for M = 500, σ = 1/4 and various n_r and n_s. Note that the curves intersect for $n_r - n_s$ = 1,2, etc., the points of intersection lying along straight lines of slope one. Since $n_r - n_s = n+m$, we see that the intersections of the resonance curves are just the fixed points (I_{nm}, J_{nm}). These curves are of central importance in the ECRH problem, as orbits tend to diffuse along them, and we have therefore studied their properties in detail. It is easily shown that the maxima of J_s lie along the line $I = \frac{5}{2}J$ and that the maxima of I_s lie on the I-axis, i.e., the n_s curves cross the I-axis horizontally. The region $I > J$ is specifically excluded in iterating the mapping, since $v_\perp^2 > 0$ there; however, I and J are both allowed to go negative.

For $J = 0$ we can also locate s-fold and r-fold fixed points in the limits $\epsilon \to 0$ and $\epsilon \to \infty$, respectively, as in the two-frequency Fermi mapping. Taking $J = 0$ in (44) gives

$$I_{n_s} = \frac{s^2 I_0}{n_s^3} \tag{47}$$

$$I_{n_r} = \frac{r^2 I_0}{n_r^3}.$$

Note that these fixed points are period-one in the variables $s\phi$ and $r\phi$, respectively. These islands have period p and q, where p/q is s/n_s or r/n_r reduced to lowest terms. The fixed points (47) persist for $0 > \epsilon > \infty$, just as in the Fermi mapping, but it is not known whether analogous fixed points exist for $J \neq 0$.

B. Resonance Widths

A non-stochastic orbit initially near a resonance curve will librate about the local resonance (P_r, J_r) with an amplitude which may carry it into the sphere of influence of another resonance. Knowledge of these libration amplitudes, or *resonance widths* enables us to predict the form of the adiabatic barrier in the P-J plane.

In this section we calculate widths for the principal resonances (44) using the method of averaging. The details of this calculation are given in Appendix B. The motion near one s-fold resonance is shown there to be described by the Hamiltonian

$$H = -\frac{M}{u}(2P-\sigma J) + 2\pi n_s P + \frac{1}{N}\cos\psi. \tag{48}$$

Since χ is absent, J is a constant of the motion, so that the orbit oscillates vertically about one of the s-fold resonance curves in Fig. 8. Over most of a given curve the amplitude may be found by Taylor-expanding (48) about P_r to obtain

$$H = \frac{1}{2} G(\Delta P)^2 + \frac{1}{N}\cos\psi \tag{49}$$

where

$$G = \frac{\partial^2 H_0}{\partial P^2} = \frac{-2P+5\sigma J}{4u^5} \tag{50}$$

and we have defined

$$H_0 = -\frac{M}{u}(2P-\sigma J).$$

From (49) one easily finds an expression for the separatrix, which yields the half-amplitude

$$\Delta P_{\max} = \left(\frac{2}{NG}\right)^{1/2}. \tag{51}$$

The difficulty with this approximation is that $G \to 0$ at the extremum of the resonance curve, where $J = J_{\max}$. In this region the upper and lower branches of a resonance interact strongly, first reconnecting and then annihilating. This problem has been considered by Howard and Hohs[15] and the application to the present problem is described in Appendix B. A corrected set of widths is shown in Fig. 9 for $M = 100$, $\sigma = \frac{1}{4}$, $\epsilon = 1$, and several values of n_s. Note that the widths vanish when $J = J_{\max}$.

The calculation of the r-fold resonance amplitudes is complicated by the fact that $\bar{J} = J - P/\lambda$ is a constant of the motion, rather than J itself. Consequently the libration is along the direction $P/J = \lambda$. After some manipulation one finds a simple equation for the amplitude,quite similar to the s-fold width, as described in Appendix B. Figure 10 shows a set of r-fold widths for the same parameters used in Fig. 9. Overlaying these two figures accurately determines the barrier to stochastic motion, as described in the next section.

C. Adiabatic Barrier

We wish to estimate the manner in which KAM surfaces limit heating from below in the action space (I,J). For small J, the approximate two-dimensional mapping derived in Sec. II.B gives a useful expression for the KAM barrier based on the overlap of neighboring island chains. For the complete four dimensional mapping we can obtain an approximate barrier by writing a local two-dimensional map for each value of J and applying the two-thirds rule to compute $I_B(J)$. The complete barrier for $\epsilon = 1$ is then given approximately by the upper edge of the set of overlapping resonance bands in Fig. 10a-b. Strictly speaking, a factor of 3/2 should be used in computing the resonance widths to conform to the two-thirds rule for overlap, but is omitted here. This is partially compensated for by the fact that the resonance widths in Fig. 9-10 are calculated assuming all of the power is in each frequency (N=1). Figure 10 shows the results of a number of single orbits for $\epsilon = 1$, initialized 5 units above the $I = J$ line at intervals $\Delta J = 2.5$. Superimposed are the resonance width curves from Figs. 9-10. The upper bound of the data is seen to closely follow the calculated upper edge of the overlapping resonance bands. Arnold diffusion can cause penetration of this barrier but as we shall show in Sec. V, the time scale for this process is much longer than the times corresponding to the numerical data.

V. Intrinsic Diffusion

A. Quasilinear Diffusion

In the region of strong resonance overlap, the motion is chaotic and can be described by a Fokker-Planck equation in the actions alone. Letting $f(\mathbf{I},n)$ be the distribution function of the action $\mathbf{I} = (I,J)$ at time step n, we have

$$\frac{\partial f}{\partial n} = -\frac{\partial \Gamma}{\partial \mathbf{I}} \tag{52}$$

where

$$\Gamma = -\mathbf{D} \cdot \frac{\partial f}{\partial \mathbf{I}} \tag{53}$$

is the flux and $\mathbf{D}$ is the diffusion tensor. Making the random phase (quasilinear assumption, the components of $\mathbf{D}$ are

$$\begin{aligned} D_{II} &= \langle(\Delta\, I)^2\rangle_{\phi\chi} \\ D_{IJ} = D_{JI} &= \langle \Delta I \Delta J \rangle_{\phi\chi} \\ D_{JJ} &= \langle(\Delta J)^2\rangle_{\phi\chi} \end{aligned} \tag{54}$$

where $\langle\ \rangle_{\phi\chi}$ denotes the average over both ϕ and χ and $\Delta I = I'-I$, $\Delta J = J'-J$ in (24). After averaging, we obtain

$$\begin{aligned} D_{II} &= \frac{s^2}{2N^2}(1+\epsilon^2\lambda^{2)} \\ D_{IJ} &= \frac{\epsilon^2 s\,\lambda}{2N^2} \\ D_{JJ} &= \frac{\epsilon^2}{2N^2}. \end{aligned} \tag{55}$$

To obtain isotropic diffusion we introduce the skewed coordinates

$$y = \epsilon\,\frac{I}{s} - \epsilon\lambda J \tag{56}$$

$$x = J.$$

Using (24), we find

$$\Delta\, y = \frac{\epsilon}{N}\sin(s\phi), \tag{57}$$

$$\Delta\, x = \frac{\epsilon}{N}\sin(r\phi+\chi),$$

and averaging over the angles we obtain the isotropic tensor

$$D_{xx} = D_{yy} = D_0 = \frac{\epsilon^2}{2N^2} \tag{58}$$

$$D_{xy} = 0.$$

These results will be used in Sec. VI to investigate enhanced axial losses due to diffusion into a mirror loss cone.

A numerical calculation of the diffusion tensor has been made in order to verify the quasilinear assumption. Figure 12 shows $\sigma^2 D_{II}$, σD_{IJ} and D_{JJ} versus the number of timesteps n for 1000 initial conditions with random phases at $I_0 = 100$ and $J_0 = 10$. These initial conditions are well within the region of strong resonance overlap for the chosen system parameters M = 2 x 10^4, $\epsilon = 0.8$, r = 5 and s = 4. The quasilinear values (solid lines) are seen to lie close to the computed data for small n. For large n there is a tendency for the computed value of D_{II} to fall below its quasilinear value. This is due to the presence of a reflecting barrier at $u = 0 (I \approx J_0 = 10)$. For $n \geqslant (I_0 - J_0)^2/(2D_{II}) \approx 500$ the computed mean square displacement $<(\Delta I)^2>$ is reduced by these reflections. Indeed, since $D_{JJ} << D_{II}$ and there also exists an adiabatic barrier at large $I [I_B \approx 1860$ from Eqs. (23) and (29)], $<(\Delta I)^2>$ cannot grow indefinitely. Thus the computed value of D_{II} must fall as n^{-1} for large n.

B. Thin Layer Arnold Diffusion

For four dimensional mappings such as (24), an initial condition chosen within the thick stochastic layer ($I-J \gtrsim 0$) can diffuse above the adiabatic barrier. This process, known as Arnold diffusion, can provide a mechanism for heating particles above the barrier.

To calculate the Arnold diffusion rate, we use the three-resonance stochastic pump model[12] in a region above the adiabatic barrier, I_B, where the resonances do not overlap. For convenience and to maximize the diffusion rate we choose a "guiding" resonance just above the adiabatic barrier and use initial conditions having $J << I$. The stochastic motion along this isolated resonance (mainly along J) is known as "thin layer" Arnold diffuson and is driven by the interaction of the two resonances nearest in frequency to the guiding resonance.

As an example we calculate the Arnold diffusion coefficient along the isolated guiding resonance

$$r\dot{\phi} + \dot{\chi} + 2\pi n_r = 0, \tag{59}$$

which lies between the two nearest "driving" resonances

$$s\dot{\phi} + 2\pi n_s = 0, \tag{60}$$

and

$$s\dot{\phi} + 2\pi(n_s + 1) = 0 . \tag{61}$$

The calculation involves several canonical transformations and is given in Appendix C. From Eq. (C20), we derive the diffusion coefficient D_A for the diffusion of the transformed action $\bar{J}$ [see Eq. (C7)] which is conserved in the absence of Arnold diffusion.

We compare this result with a numerical calculation of D_A obtained by iterating the mapping (24) for a set of 20 initial conditions having slightly different phases but the same values of I and J. We choose $M = 240$, $n_r = 7$, $n_s = 5$, $r = 5$, $s = 4$, and $\epsilon = 3$. This places the guiding resonance n_r just above the adiabatic barrier and approximately midway between the two guiding resonances n_s and n_s+1. These choices lead to a reasonably large diffusion rate. As shown in Fig. 13, after about 10^4 iterations of the mapping, the numerical value of D_A settles down to approximately 5 x 10^{-6}, where it remains for the 10^6 iterations of the map which were explored numerically. The initial transient behavior of D_A arises because $\bar{J}$ is only approximately a constant of the motion for the complete mapping which contains many (not just three) resonances. From Eq. (C20), the analytical value of D_A is 6.2 x 10^{-5} . This is not unreasonable, considering the limitations of the three resonance theory (see for example Ref. 12) and the sensitive exponential dependence of the analytical result on the linearized frequency of the guiding resonance and the frequency separation between the guiding and driving resonances. These frequencies were chosen to maximize the diffusion rate in the analytical theory.

VI. Enhanced Axial Loss due to Intrinsic Diffusion

We now consider the enhanced loss that results when a loss cone with mirror ratio R_L is present for two-frequency ECRH. For heating at a single frequency with local mirror ratio $R_1 < R_L$, the heating acts to increase the local $E_\perp$, while the local $E_\parallel$ remains unchanged. The addition of a second heating frequency causes a diffusion in $E_\parallel$. If $\Delta E_\parallel$ becomes large enough, then the particle will turn at $R > R_L$ and be lost from the confinement region. This mechanism may be much stronger than classical pitch angle scattering in producing diffusion of $E_\parallel$.

To examine this process, we consider quasilinear diffusion of $E_\perp$ and $E_\parallel$ using the ideal mapping (24). For these equations, $E_\perp$ and $E_\parallel$ are related to I and J through Eqs. (14), (15), and (23). Transforming to variables x,y given by (4.5) in which the quasilinear diffusion tensor is isotropic, we consider the two-dimensional steady state model problem illustrated in Fig. 14. Here the distribution function f satisfies Laplace's equation, which in cylindrical geometry is

$$\frac{1}{r}\frac{\partial}{\partial r}\left(r\frac{\partial f}{\partial r}\right)+\frac{1}{r^2}\frac{\partial^2 f}{\partial\theta^2}=0 \tag{62}$$

where $y = r\cos\theta$, $x = r\sin\theta$. A delta function source is assumed to exist at $r = d$, $\theta = \theta_1$, and a simple form for the adiabatic barrier to heating is chosen; namely, a circular boundary at $r = r_B$. This boundary is assumed to perfectly reflect particles; i.e., $\partial f/\partial r = 0$ at $r = r_B$. The choice of a circular boundary is a crude approximation to the actual shape of the adiabatic barrier, and will be justified later. To model the exponential decrease in the Airy functions for $E_\parallel < 0$, a perfectly reflecting barrier is chosen at $x = 0$, i.e., $\partial f/\partial\theta = 0$ at $\theta = \pi/2$. The loss cone boundary is found from conservation of energy and magnetic moment

$$E_\perp + E_\parallel = E_{\perp L},$$

$$\frac{E_\perp}{R_1} = \frac{E_{\perp L}}{R_L},$$

which yields

$$E_\parallel - \rho_L E_\perp = 0, \tag{63}$$

where $\rho_L \equiv R_L/R_1 - 1$. Transforming (63) to the x,y variables (56), we obtain the loss cone boundary

$$y = -\epsilon(1-\lambda_L)x, \tag{64}$$

where

$$\lambda_L \equiv \frac{\delta\omega}{\omega_1}\frac{1}{\rho_L} \tag{65}$$

is typically much less than unity.

In describing the particle loss at the loss cone boundary, we must take into account the finite step size of the ECRH diffusion process. In the absence of a loss cone ($R_L \to \infty$), we have reflected all particles which step below the $E_\perp = 0$ line

$$y = -\epsilon x \tag{66}$$

when numerically iterating the simplified mapping (24). When a loss cone is present, some particles may step into the loss cone region and be lost, but others may step across the loss cone region below the $E_\perp = 0$ line and thereby be reflected. To model this process, we first estimate the value x_0 on the loss cone boundary above which all particles stepping across the boundary are lost and none reflected. From (57), the maximum step across the loss cone boundary is $r\Delta\theta = \epsilon/N$. The arc length between the loss cone boundary (64) and the $E_\perp = 0$ line (66) is, for $\lambda_L << 1$,

$$r\Delta\theta = \frac{\epsilon\lambda_L x}{(1+\epsilon^2)^{1/2}}.$$

Equating these two lengths we obtain

$$x_0 = \frac{(1+\epsilon^2)^{1/2}}{N\lambda_L}. \tag{67}$$

For $x > x_0$, all particles which step across the loss cone boundary are lost. For $x < x_0$, a fraction proportional to the ratio x/x_0 are lost. One model for the loss cone boundary condition is to choose $f = 0$ for $x > x_0$ and approximate the boundary condition for $x < x_0$ as

$$\frac{x}{x_0} D_0^{1/2} f - D_0 \frac{1}{r} \frac{\partial f}{\partial \theta} = 0. \tag{68}$$

Equation (68) yields the proper "thermal" flux for $x = x_0$ while making the flux vanish for $x << x_0$. However, this leads to a mixed boundary value problem which can only be solved numerically. We opt for a simpler approach by choosing $f = 0$ everywhere on the loss cone boundary. After obtaining f analytically, we decrease the particle and energy fluxes across the loss cone boundary by the ratio x/x_0 for $x < x_0$. These fluxes are then used to determine the mean loss rate ν_L and the mean energy E_L of a lost particle. This procedure yields reasonable values for ν_L and E_L and allows the scaling of ν_L and E_L with the system parameters to be obtained analytically. The procedure is justified by comparing ν_L and E_L with the results of a numerical simulation of the loss process.

The solution to the boundary value problem is given in Appendix D. The average energy lost per particle is found from (D16) and (D17);

$$E_L = \frac{P_L}{S_L},$$

and the mean loss rate from (D16) and (D18),

$$\nu_L = \frac{S_L}{N}.$$

To compare these with the results of numerical simulation, we have chosen $\epsilon = 1$. In this case, from (D2) and (D7), $\theta_0 = \pi/4$ and $\alpha_0 = 2/3$. Then $J_L = E_L/\Delta$ and $\tau_L = \nu_L^{-1}$ are given by

$$J_L = \frac{2}{3} r_0^{2/3} r_B^{1/3} \left[\frac{1-\frac{3}{4}(\frac{r_0}{r_B})^{1/3}}{1-\frac{1}{3}(\frac{r_0}{r_B})^{1/3}} \right], \tag{69}$$

$$\tau_L = \frac{3}{8D_0} r_0^{2/3} r_B^{4/3} \left[1-\frac{1}{3}(\frac{r_0}{r_B})^{2/3} \right]^{-1}, \tag{70}$$

for $r_0 < r_B$; and by

$$J_L = \frac{1}{4} r_B \tag{71}$$

$$\tau_L = \frac{9}{16D_0} r_B \, r_0 \tag{72}$$

for $r_0 > r_B$.

For the important case $r_B > r_0$, we see from (69) that $J_L \propto r_B^{1/3}$. Thus, the exact location or shape of the adiabatic barrier is not important in determining the average energy lost per particle. However, $\tau_L \propto r_B^{4/3}$ and therefore the mean loss time more than doubles if r_B is doubled. This variation arises because f decays slowly ($\propto r^{-2/3}$) in the wedge. Thus, as r_B increases, for a fixed source, the particle number N increases, leading to longer confinement times.

The actual adiabatic boundary is determined from resonance overlap conditions as described in Sec. IV C. A numerical example of a thick layer stochastic region bounded by an adiabatic barrier is shown in Fig. 15. It consists of a large block for $J \lesssim 20$ and a strip lying between the lines $I = J$ and $I \approx J + 30$ for $J \gtrsim 20$. When this region is transformed to the x,y space the block transforms roughly to a $135°$ wedge having mean radius $r_B \approx 15$, and the strip transforms to a strip lying between $y = -x$ and $y = 7.5 - x$ that is attached to the wedge. Since $f = 0$ on the boundary $y = -x$ of the strip, f decays away from the wedge into the strip with characteristic e-folding distance $2w/\pi$ where $w \approx 5$ is the width of the strip. Thus, the total number of particles stored in the strip is small compared to the number stored in the wedge, and the presence of the strip may be neglected. A circular boundary is thus a reasonable choice for the adiabatic barrier in Fig. 14.

To compare the theory with numerical results we choose $\epsilon = 1$ $(\theta_0 = \pi/4)$, $\lambda = \frac{5}{4}$ and $\lambda_L = \frac{1}{16}$, the latter corresponding to a loss cone edge, using (64) and (56), at $I = 1.25J$. We then obtain from (67) $x_0 \approx 14.1$ and $r_0 = x_0 \sec\theta_0 \approx 20.0$. From (29) and using (56), the adiabatic barrier for $J = 0$ is at $y_B = (M/2)^{2/3}$. We estimate that the effective radius of the wedge is $1/\sqrt{2}$ times this value; $r_B \approx 0.44 M^{2/3}$. For these values of r_0 and r_B, we determine J_L and τ_L from (69) - (72) for various values of M. The results are shown as the solid lines in Fig. 16.

For the numerical computations, we determine J_L and τ_L for the initial conditions $I = 10, J = 1$, with initial angles chosen at random. Up to 500 different initial conditions were used to obtain average values for J_L and τ_L. Each initial condition was iterated using the map (24). Particles which stepped below the loss cone edge $I = 1.25J$ were reflected in I if they also stepped below the $E_\perp = 0$ line $I = J$, and were removed (and computation ended) if they fell into the loss cone between the $I = 1.25J$ and $I = J$ lines. Particles stepping into the $J < 0$ region were reflected in J, corresponding to the condition that the particles do not turn before reaching the resonance zone. The numerically calculated values are shown as circles in Fig. 16. The agreement with theory is reasonably good for both J_L and τ_L, the latter quantity being somewhat sensitive to details of the dynamics near the adiabatic barrier. These results will be compared with collisional losses in Sec. VIII B.

VII. Modifications Required for ECRH Mappings

In this section we consider some implications of our results for ECRH experiments. In order to do this we must re-introduce certain features of the ECRH problem that are not included in the idealized mappings of the previous sections. In particular, the $E_\perp$ and $E_\parallel$(P and J) dependence of the energy perturbations must be considered.

A. Improved Mapping

We consider as before the heating approximation in which the net kick that a particle receives both on entering a resonance zone and on leaving after reflection is lumped into a single value. Then a Taylor expansion of the magnetic field in the neighborhood of the turning point leads to the kick at a resonance zone (expressed in local variables at the resonance point),

$$\delta E_\perp = 4\pi \frac{e}{m} \mathcal{E} \left[\frac{2B}{(dB/dz)_t \omega^{1/2}} \right]^{2/3} J_0(k_\perp \rho) \, E_\perp^{1/6} Ai(x) \sin \psi \tag{73}$$

where $\mathcal{E}$ is the electric field amplitude, the subscript t denotes evaluation at the turning point, unsubscripted variables are evaluated at the resonance point, $k_\perp$ is the perpendicular wave number, ρ is the gyroradius, Ai is the Airy function, and

$$x = -(\Omega_t - \omega) \left[\frac{2B}{v_\perp \omega^{1/2} (dB/dz)_t} \right]^{2/3} . \tag{74}$$

Henceforth we assume $k_\perp \rho << 1$ and so replace J_0 by 1.

We add together the effects of two frequencies, transforming the kick in $E_\perp$ due to the second frequency to $E_\perp, E_\parallel$ variables at the first resonance point as in Sec. II. The result is

$$E'_\perp = E_\perp + \alpha \left[\mathcal{E}_1 Ai(x_1) \sin \psi + \mathcal{E}_2 \left(\frac{B_1}{B_2} \right)^{1/2} Ai(x_2) \sin(\psi + \xi) \right] \tag{75}$$

$$E'_\parallel = E_\parallel + \alpha \frac{\delta\omega}{\omega_1} \mathcal{E}_2 \left(\frac{B_1}{B_2} \right)^{1/2} Ai(x_2) \sin(\psi + \xi)$$

where

$$\alpha = 4\pi \frac{e}{m} \left[\frac{2B_1}{(dB/dz)_t \omega_1^{1/2}} \right]^{2/3} E_\perp^{1/6} \tag{76}$$

and subscripts 1, 2 denote evaluation at the first or second resonance point, respectively. The variables ψ and ξ evolve as in Eqs. (9) and (11). The Airy function $Ai(x)$ has three regions of interest: (1) For turning in the resonance zone (-1 < x < 0) the Airy function is approximately constant. Then $\Delta E_\perp \propto E_\perp^{1/6}$, giving a slightly different mapping from Eqs. (19); (2) For particles turning before resonance (x > 0) the Airy function decays exponentially as

$$Ai(x) \propto x^{-1/4} \exp\left(-\frac{2}{3} x^{3/2}\right), \quad x >> 1 \tag{77}$$

resulting in a rapid drop of the interaction strength of a second resonance at higher frequency. (3) For particles penetrating deeply through resonance (-x >> 1), $Ai(x)$ oscillates about zero. For a single frequency and single wave-vector the Airy function zeroes can prevent certain classes of particles from being heated. However, when -x >> 1 the "lumped" approximation fails; treatment of resonant interactions before and after reflection as separate kicks leads to the conclusion that Airy-function zeroes are barriers to diffusion only at energies near the adiabatic barrier. These phenomena and their implications for heating are discussed below.

For all the above cases the mappings given by Eqs. (75), (9) and (11) are not area preserving. This leads to spurious effects associated with dissipative mappings, not consistent with the Hamiltonian nature of the ECRH physics. This problem arises because the phase-advance equations are not calculated to sufficient accuracy. Stated another way, the derived approximate mapping is only approximately area-preserving,

$$J \equiv \left| \frac{\partial(E_\perp', \frac{\omega}{\delta\omega} E_\parallel', \psi', \xi')}{\partial(E_\perp, \frac{\omega}{\delta\omega} E_\parallel, \psi, \xi)} \right| = 1 + O\left\{ E_\perp \frac{\partial[\ln \alpha Ai(x)]}{\partial E_\perp} \right\} \tag{78}$$

whereas the exact equations are exactly area preserving. In doing numerical experiments it is important to maintain area preservation in order not to introduce qualitative changes in the solution. This has already been noted in connection with a two-dimensional ECRH study[5]. Area preservation can be maintained by adding appropriate first-order phase-dependent terms to the phase advance equations. Then, following Sec. II, we introduce the slowly varying phase $\chi \equiv \xi - (2\delta\omega/\omega\rho)\psi$ and transform the (now canonical) variables $(E_\perp, (\omega/\delta\omega)E_\parallel, \psi, \xi)$ to the normalized set (P, J, ψ, χ) where $E_\perp = C(P-\sigma J)$, $E_\parallel = C(\delta\omega/\omega)J$, and

$$C \equiv \left[Ai(0)\,\frac{4\pi e}{m} \right]^{6/5} \left[\mathcal{E}_1^2 + \mathcal{E}_2^2\,\frac{B_1}{B_2} \right]^{3/5} \left[\frac{2B_1}{(dB/dz)_1 \omega_1^{1/2}} \right]^{4/5}. \tag{79}$$

The result is:

$$\begin{aligned}
P' &= P + \frac{(U')^{1/3}}{N} [ai_1 \sin\psi + \epsilon\lambda\, ai_2 \sin(\lambda\psi + \chi)] \\
J' &= J + \frac{(U')^{1/3}}{N}\,\epsilon \sin(\lambda\psi + \chi) \\
\psi' &= \psi - \frac{M}{u'} + \frac{\sigma M J'}{2u'^3} + (APT)'_\psi \\
\chi' &= \chi - \frac{\sigma^2 M J'}{2u'^3} + (APT)'_\chi
\end{aligned} \tag{80}$$

where

$$M = \frac{\pi R_1^{1/2}\,\omega_1 L\rho}{2\left[Ai(0)\frac{4\pi e}{m} \right]^{3/5} \left[\mathcal{E}_1^2 + \mathcal{E}_2^2\,\frac{B_1}{B_2} \right]^{3/10} \left[\frac{2B_1}{(dB/dz)_1 \omega_1^{1/2}} \right]^{2/5}} \tag{81}$$

and $\epsilon = (\mathcal{E}_2/\mathcal{E}_1)(B_1/B_2)^{1/2}$, $N^2 = 1 + \epsilon^2\lambda^2$, $u^2 = P - \sigma J$, $U = u^2/(P - \sigma J/2)^{1/2}$, $ai_j = Ai(x_j)/Ai(0)$, and the area-preserving terms are

$$\begin{aligned}
(APT)_\psi &= -\frac{1}{N}\frac{\partial}{\partial P}(U^{1/3} ai_1)\cos\psi - \frac{\epsilon}{N}\frac{\partial}{\partial P}(U^{1/3} ai_2)\cos(\lambda\psi + \chi) \\
(APT)_\psi &= -\frac{1}{N}\frac{\partial}{\partial J}(U^{1/3} ai_2)\cos(\lambda\psi + \chi).
\end{aligned} \tag{82}$$

Note that in these variables the arguments of the Airy functions are

$$\begin{aligned}
x_1 &= -(2M/\pi)^{2/3}\,\frac{\sigma J}{2u^2(P-\sigma J/2)^{1/3}} \\
x_2 &= -(2M/\pi)^{2/3}\,\frac{\sigma(J-u^2)}{2u^2(P-\sigma J/2)^{1/3}}.
\end{aligned} \tag{83}$$

We now discuss in more detail the consequences of the modified map (80).

B. Scaling Considerations

For practical applications of the calculation of the KAM barrier to heating for one or more frequencies we use the scaled ECRH mapping, Eq. (80), for $-1 < x < 0$, and consider the behavior near $J = 0$ (turning at resonance). The small area-preserving phase correction terms may be ignored in making analytic estimates of heating barriers. For a single frequency and $J = 0$, the resulting two dimensional mapping in a parabolic well is

$$\Delta P = P^{1/6} \sin \psi$$

$$\Delta\psi = \frac{M}{P^{1/2}} \tag{84}$$

where

$$M = \frac{\pi R^{3/10} \rho^{6/5}}{2[8\pi Ai(0)]^{3/5}} \Lambda^{3/5}. \tag{85}$$

with Λ a dimensionless parameter which varies with experimental parameters,

$$\Lambda = \frac{m\omega^2 L}{eE} \quad . \tag{86}$$

Note that the definitions of M and P differ from those in Sec. II.

As in Sec. IV we obtain the normalized barrier energy from the two-thirds rule, (27). For a single frequency with $J = 0$ this reduces to (28), which for the mapping (80) gives

$$P_B = (M/2)^{3/4} \tag{87}$$

The power of the M dependence is different from that in (29).

As in Sec. II we can also make a simple estimate of the maximum increase in the heating barrier that can be achieved by dividing the available power between two frequencies. In this case, resonances 1 and 2 in (27) are the interspersed resonances of the two frequencies. At a given value of action the interspersal halves the distance between resonances and the constant power condition reduces the resonance size by $2^{1/4}$. Since $\delta P \propto P^{3/2}$ and $\Delta P \propto P^{5/6}$, (27) is marginally satisfied at a ratio of final to initial values of P given by

$$\left(\frac{P_{fB}}{P_{iB}}\right)^{5/6} = 2^{-3/4}\left(\frac{P_{fB}}{P_{iB}}\right)^{3/2} \tag{88}$$

which gives an increase in action (energy) at the barrier

$$\frac{P_{fB}}{P_{iB}} = 2^{9/8}. \tag{89}$$

C. Overlap of Resonance Zones

Because the particles tend to turn within the inner (lower frequency) resonance zone the effect of the outer (higher frequency) resonance is diminished by the exponential fall-off of the effective energy kick. Therefore, an additional condition to be satisfied for two frequency heating is that the interaction zones of the two resonances overlap. That is, we must have $x \lesssim 1$ for the outer resonance at the turning point corresponding to the inner resonance. Since

$$\omega_2 = \omega_1 \left(1 + \frac{1}{B}\frac{dB}{dz}\Delta z\right)$$

we have, using (74),

$$\frac{\Delta\omega}{\omega} = x\left(\frac{1}{B}\frac{dB}{dz}\frac{v_\perp}{2\omega}\right)^{2/3}. \tag{90}$$

Substituting (85) for M (parabolic mirror) in (90) then gives

$$\frac{\Delta\omega}{\omega} = \frac{b^{2/3}}{c}\frac{P^{1/2}}{M^{2/3}}x \tag{91}$$

where

$$b = \frac{R^{3/10}\left(1-\frac{1}{R}\right)^{6/5}}{2[8\pi Ai(0)]^{3/5}}, \quad c = \frac{\left(\frac{R^2}{R-1}\right)^{1/3}}{[4\pi Ai(0)]^{2/3}}.$$

To find the value of $\Delta\omega/\omega$ at the adiabatic barrier for a single frequency, we use (91) to obtain

$$\frac{\Delta\omega}{\omega} = \frac{b^{2/3}}{2^{1/4}c}\frac{|x|}{M^{5/12}}. \tag{92}$$

Requiring that $|x| \leqslant 1$ and taking a model problem with $R = 2$, (92) becomes

$$\frac{\Delta\omega}{\omega} \lesssim \frac{0.5}{M^{5/12}}. \tag{93}$$

We have previously derived an interspersal formula for $r = s+1$ and $n_r = n_s+m$, where n_s and n_r are the number of 2π phase shifts per mapping period (1/2 bounce period), which for large n_s is

$$s = \frac{2n_s}{2m-1} \quad .$$

Letting $m = 1$, $n_s = s/2$, and using the fixed point condition

$$\frac{M}{P^{1/2}} = 2\pi n_s$$

together with the barrier condition (87) we obtain

$$s = \frac{2^{3/8}}{\pi} M^{5/8}. \tag{94}$$

Combining (93) and (94) and observing that $s = [(R-1)/2R]\omega/\Delta\omega = \omega/(4\Delta\omega)$ we obtain the range of M for which spatial overlap of resonance zones occurs, while simultaneously giving island interspersal at the barrier. We find $M \geqslant 28$, which is satisfied for machines of current interest (see Table 1 below), and does not present a serious restriction on device parameters.

Table 1 gives the derived values of M, the maximum $\Delta\omega/\omega$ for overlap of resonances zones, the corresponding σ, P_B, and barrier energy $E_{\perp B}$ for parameters representative of STM and MFTF-B. Note that for MFTF-B the calculated barrier energy is relativistic, although the map (80) is nonrelativistic.

D. Effect of Zeroes of Airy Functions

For particles turning beyond resonance, the argument x of the Airy function in Eq. (73) is negative and so Ai(x) oscillates as a function of x. In particular, Ai(x) has an infinite set of zeroes x_k, which arise from interference between the velocity kicks a particle receives upon crossing the resonance zone before and after turning. Mathematically the Airy function is obtained from perturbation theory in which the equations of motion are integrated through both resonance passages, ignoring local variations in $E_{\perp}$, and $E_{\parallel}$ (P and J). In terms of a two-step model with discrete kicks before and after turning, the Airy-function approximation corresponds to calculating the phase slip $\delta\psi$ between the two kicks neglecting the change in (P,J) that occurs at the first kick. Consequently, the condition for complete destructive interference (k^{th} zero of the Airy function) is that P be a certain function of J, $P = P_k(J)$, independent of ψ, χ and the wave amplitude. Thus for single-frequency (ω_1) heating in this approximation, $P = P_k(J)$ is a KAM curve in the $P-\psi$ phase plane, independent of the wave amplitude, and so always constitutes a barrier to diffusion. Furthermore, for any finite wave amplitude (finite M), there is a non-stochastic layer about $P = P_k$ given approximately by the condition $K(P) < 1$, where K is the Chirikov parameter $K = (\Delta P/\sin\psi)\partial\Delta\psi/\partial P$. In P-J space, the family of curves $P=P_K(J)$ in general intersect the heating characteristics (J = const. for the case $\epsilon = 0$) at finite angles, and so constitute barriers to diffusion. In this approximation, adding a second frequency has a profound effect: the zeroes of $Ai(x_2)$ are not coincident with those of $Ai(x_1)$ except at isolated points in P-J space; thus a particle can diffuse across a xero of one Airy function under the influence of the second frequency. The diffusion is merely reduced from two-dimensional (in $P-J$ space) to one-dimensional near a zero of an Airy function. This is the basis for Samec's interpretation of the effect of multiple frequencies[8].

In a more complete picture nonlinear effects lead to a destructive interference condition which depends on ψ, χ and the wave amplitude. In the two-step model, $\delta\psi$ depends on ψ, χ and the wave amplitude. Consequently, the condition for net zero displacement after both passages through resonance is now $P = P_k(J,\psi,\chi)$, and is no longer guaranteed to be a KAM curve. Studies of asymmetric two-step maps indicate[16] that the non-stochastic band about $P = P_k$ disappears and $P = P_k$ ceases to be a KAM curve approximately when the step size (maximized over ψ) for a single step of the map exceeds the width of the K < 1 layer calculated by combining two successive steps and neglecting the intermediate change in P (the Airy-function approximation for ECRH).

To apply this criterion to the ECRH problem, we must (1) calculate the width of the K < 1 region in the Airy-function approximation, and (2) evaluate the step δP on a single passage through the resonance zone. We do this here for the ω_1 resonances and $\sigma J \ll P$. To determine the width of the K < 1 region about the zero of the Airy function, we first determine K from Eqs. (80) with $\epsilon = 0$,

$$K = \left|\frac{\Delta P}{\sin\psi}\frac{\partial\Delta\psi}{\partial P}\right| = \frac{1}{2}M\, P^{-4/3} ai_1 \ .$$

We assume $MP^{-4/3} \gg 1$ and so calculate the width of the K = 1 region about a zero of ai_1 by Taylor expansion of the Airy function. Hence

$$(\Delta P)_{K=1} \cong \frac{2}{M}\frac{P^{4/3}}{|ai_1'(dx_1/dP)|} \tag{95}$$

$$= \frac{3}{2M}\frac{P^{7/3}}{|xai_1'|}$$

where ai'_1 denotes $d(ai_1)/dx$. To calculate the change δP due to a single passage through resonance, we integrate the equations of motion after expanding about the resonance point rather than the turning point. The resulting counterpart to Eq. (73) is [see, e.g., Ref. (19)]

$$\delta E_\perp = 2\pi^{1/2}\frac{e}{m}E\frac{(2B_1)}{\omega_1(dB_1/dz)^{1/2}}\frac{E_\perp^{1/2}}{E_\parallel^{1/4}}\sin\psi \ . \tag{96}$$

Converting to P,J variables, taking the peak amplitude of sin ψ, and again evaluating for $\sigma J \ll P$, we find:

$$\delta P = \frac{P^{1/6}}{2\pi^{1/2} Ai(0)|x|^{1/4}} \; . \tag{97}$$

If we now track a particular zero of the Airy function we observe that δP is less than $(\Delta P)_{K=1}$, and thus the Airy function should constitute a barrier to diffusion if P is greater than P_c, where

$$P_c = \frac{|x|^{9/26}(ai_1^{'})^{6/13}}{\pi^{3/13}[3Ai(0)]^{6/13}} \; . \tag{98}$$

It is useful to compare P_c with the stochastic-barrier energy at $J = 0$, $P_B = (M/2)^{3/4}$. For the first zero of the Airy function, we find x=2.34 , $P_c/P_B = 0.31$ for $M = 10^3$ and 0.16 for $M = 10^4$, while for the fifth zero, $x = 7.94$, $P_c/P_B = 0.55$ for $M = 10^3$ and 0.28 for $M = 10^4$. On the other hand, we recall that stable fixed points surrounded by adiabatic islands exist, even in the $J = 0$ map, for $P > P_B/4$. Thus, for STM parameters, as P is increased, Airy function zeroes start to become barriers to diffusion at roughly the same energy as that at which a significant portion of the phase space away from Airy-function zeroes becomes non-stochastic.

VIII. Comparison of Intrinsic and Collisional Diffusion

A. Diffusion into the Loss Cone

Using the results of Sec. VI, we calculate the rate of intrinsic diffusion into the loss cone for a practical ECRH configuration. We use the mapping (80) but in the simpler form in which the Airy functions are evaluated at zero argument and the associated area-preserving terms in the phase equations are neglected. We can then approximately modify (69) and (79) to new values (with tildas), which, for $\tilde{r}_0 << \tilde{r}_B$ give

$$J_L = \frac{2}{3}\,\tilde{r}_0^{2/3}\,\tilde{r}_B^{1/3} \tag{99}$$

$$\tau_L = \frac{3}{8D_0}\,\tilde{r}_0^{2/3}\tilde{r}_B^{4/3} \tag{100}$$

Using the same approximations as in Sec. VI, $r_B = \frac{1}{\sqrt{2}} P_B$ but using (91) to calculate the barrier value we find

$$\tilde{r}_B = \frac{1}{2^{1/2}}\left(\frac{M}{2}\right)^{3/4} . \tag{101}$$

Taking an average step size $\left(\frac{P_B}{2}\right)^{1/6}$ and setting $\epsilon = 1$, (58) and (101) give

$$D_0 = \frac{1}{2^{3/2}}\,\frac{(M/2)^{1/8}}{2^{1/6}} . \tag{102}$$

For the simplified problem the maximum change $\Delta P = 1$, while for the ECRH mapping (84) $\Delta P \approx P^{1/6}$. Since we find $J = J_0$ by using the relation that $E_\perp(J)$ at the loss cone edge is equal to $\Delta E_\perp$ (max), then, approximating the normalized $E_\perp$ by P and $\Delta E_\perp$ by ΔP (valid for small σ) we see that the condition $E_\perp = \Delta E_\perp$, which determines J_0, can be written

$$P(J_0) = P^{1/6}(J_0)$$

which is satisfied for $P=1$, *i.e.*, J_0 is the same as for the simplified mapping. Thus, if the slight modification of the fraction of particles falling into the loss cone that arises from the $\Delta P \propto P^{1/6}$ dependence is ignored, we obtain

$$\bar{r}_0 = 2^{1/2} J_0 = (2)^{1/2} \frac{\omega}{\delta\omega} (\frac{R_L}{R_1} - 1) \tag{103}$$

where $R_L = B_M / B_0$ and $R_1 = B_1 / B_0$.

Substituting (101) through (103) in (99) and (100) (setting $R_L/R_1 = 2$ as an example) we obtain

$$J_L \approx \frac{2}{3} (\frac{\omega}{\delta\omega})^{2/3} M^{1/4}$$

$$\tau_L \approx \frac{2^{3/2}}{8} (\frac{\omega}{\delta\omega})^{2/3} M^{7/8}$$

Returning to dimensional variables

$$E_L \approx \frac{2}{3} (\frac{\delta\omega}{\omega})^{1/3} M^{1/4} V^2 \tag{104}$$

$$\tau_L \approx \frac{2^{3/2}}{8} (\frac{\omega}{\delta\omega})^{2/3} M^{7/8} \frac{\bar{\tau}_b}{2}$$

where V, defined from the mapping equations (79) - (81), is given by

$$V = [4\pi \frac{e}{m} \mathcal{E} Ai(0)]^{3/5} \left(\frac{R_1 L^2}{\rho\omega} \right)^{1/5} \tag{105}$$

and

$$\bar{\tau}_b = \frac{1}{P_B} \int_0^{P_B} \tau_b(P)\, dP = 2\tau_b(P_B) \tag{106}$$

is an average bounce time, obtained, for a parabolic well, from (10). For STM parameters (see Table 1) we obtain $E_L \approx 63\, eV$ and $\tau_L = 1.2 \times 10^{-4}$ sec.

The particle loss time from intrinsic diffusion is considerably shorter than an average collision time in the absence of ECRH, which, for $n \approx 10^{12} cm^{-3}$ and $T_e \approx 10 keV$ yields $\tau_L \approx$

1.5×10^{-2} sec. If we take the collisional energy to be lost at the average energy $\bar{E}_\perp \approx \frac{1}{2} E_B \approx 5\,keV$, then the energy that would be lost from collisions in the absence of ECRH and the actual energy lost due to intrinsic diffusion are approximately equal.

However, this collisional mechanism is not correct for either one or two frequency ECRH. Instead, collisions, which slowly spread $E_\parallel$, combine with the more rapid $E_\perp$ diffusion to drive particles into the loss cone. In this case the $E_\perp$ intrinsic diffusion is similar for one and two frequencies. We therefore compare the intrinsic diffusion of $E_\parallel$ found from the quasilinear two-frequency result with that due to collisions in order to estimate the relative importance of the two mechanisms. The normalized quasilinear result for constant step size is, from (55),

$$<\Delta J>^2 = \frac{1}{2}(\frac{\epsilon}{N})^2. \tag{107}$$

With the heating kick proportional to $P^{1/6}$ for ECRH, this becomes

$$<\Delta J>^2 = \frac{1}{2}(\frac{\epsilon}{N})^2 P^{1/3} .$$

Reintroducing physical parameters

$$E_\parallel = V^2 \frac{\delta\omega}{\omega} J$$ (see

with velocity jump V (see Eq. 105) and step time $\tau_b/2$ the diffusion coefficient is then

$$D_{\parallel Q} = \frac{\Delta E_\parallel^2}{2\tau_b} = \frac{1}{2}(\frac{\epsilon}{N})^2 P^{1/3}(\frac{\delta\omega}{\omega} V^2)^2/2\tau_b, \tag{108}$$

An average value is then obtained by integrating over the stochastic layer distribution function f;

$$\bar{D}_{\parallel Q} = \frac{1}{P_B}\int_0^{P_B} D_{\parallel Q} f(P)\, dP$$

where P_B is the location of the adiabatic barrier near $J=0$. From (108) and taking $\tau_b \propto P^{1/2}$, (for a parabolic well) we see that $D_{\parallel Q} \propto P^{-1/6}$, and since $f(P) \approx$ const. (assuming an equilibrium is approximately reached), we find

$$\bar{D}_{\parallel Q} \approx \frac{const}{P_B}\int_0^{P_B} P^{-1/6}\, dP$$

where we have approximated the lower limit at $P = 0$ for simplicity. Integrating, we obtain

$$\bar{D}_{\parallel Q} = \frac{6}{5} D_{\parallel Q}\,(P_B). \tag{109}$$

The change in $E_\parallel$ in one mapping step due to collisions, for $E_\parallel << E_\perp$, is given by

$$<(\Delta v_\parallel)^2> = E_\perp \frac{\tau_b}{2\tau_c} \tag{110}$$

where τ_c is the electron scattering time. For small changes in $v_\parallel$ we use $\Delta E_\parallel = 2 v_\parallel \Delta v_\parallel$ to obtain

$$D_{\parallel c} = E_\parallel E_\perp / \tau_c .$$

Holding $E_\parallel$ constant and noting that $\tau_c \propto E^{3/2}$, then for $E_\parallel << E_\perp$, $D_{\parallel c} \propto P^{-1/2}$. For a given $E_\parallel$ the average can then be written

$$D_{\parallel c} \approx \frac{const}{P_B}\int_0^{P_B} P^{-1/2}\, dP$$

which yields

$$\bar{D}_{\parallel c} = 2 D_{\parallel c}(P_B). \tag{111}$$

Evaluating (109) and (111) for STM parameters, we find

$$\bar{D}_{\parallel Q} \approx 150(keV)^2/\mathrm{sec}$$

$$\bar{D}_{\parallel c} \approx 60(keV)^2/\mathrm{sec} .$$

These results indicate that the two diffusion rates are of the same order of magnitude, but the intrinsic diffusion is somewhat more rapid. In both cases the diffusion into a mirror loss cone is due to the combination of the slow parallel diffusion combined with the rapid diffusion of $E_\perp$ in the stochastic region. For single frequency ECRH this mechanism still occurs, but with only collisions driving the $E_{\parallel}$ diffusion.

B. Diffusion Through the Adiabatic Barrier

We now consider the rate of diffusion through the adiabatic barrier due to thin layer Arnold diffusion and compare the result with the diffusion expected from collisions. Following Sec. V B and Appendix C, we estimate the maximum rate of diffusion in $E_{\perp}$ by first calculating $\Delta\bar{J}$ for each mapping step and then relating this value to $\Delta E_{\perp}$ through the transformation equations. To obtain the maximum rate of Arnold diffusion we maximize the Melnikov-Arnold integral A_2 in (C19) by choosing a set of parameters such that the driving and Arnold diffusion resonances are equally spaced on either side of the guiding resonance. Since we are interspersing r and s resonances, this places the three resonances π radians apart in frequency space; i.e., the guiding resonance is midway between two resonances spaced 2π apart, and therefore the Arnold diffusion driving frequency is $\bar{\omega}_{\alpha} \approx \pi$. Furthermore, near the adiabatic barrier we expect the linearized frequency of the guiding resonance to have its maximum value $\tilde{\omega}_{\phi} \approx 1$ such that $Q = \bar{\omega}_{\alpha}/\tilde{\omega}_{\phi} \approx \pi$. The maximum value of the Melnikov-Arnold integral from (C21) is

$$A_2 = 8\pi Q e^{-\frac{\pi}{2}Q} \approx 0.6$$

From (C19) we find

$$\Delta\bar{J} = -F_2\beta^{-1}\tilde{\omega}_{\phi}^{-1}A_2 \sin\chi_0$$

which squared and averaged over all χ_0 yields

$$<(\Delta\bar{J})^2> = \frac{1}{2}\left(\frac{F_2A_2}{\beta\tilde{\omega}_{\phi}}\right)^2$$

for the diffusive change of the (otherwise) conserved actions $\bar{J}$ over a half-period of the guiding oscillation. Over a period of the mapping $(\Delta\bar{J})^2$ is reduced by the number of mapping periods in a half-period of the guiding oscillation, namely $\pi/\tilde{\omega}_{\phi}$ to give

$$<(\Delta\bar{J})^2> = \frac{\tilde{\omega}_\phi}{2\pi}\left(\frac{F_2A_2}{\beta\tilde{\omega}_\phi}\right)^2. \tag{112}$$

Using the transformations (C6) from $\bar{J}$ back to the original (I, J, W) variables and the two constraints that the diffusion lies in a resonance surface,

$$r\omega_\phi(I,\ J) + \omega_\chi(I,\ J) + 2\pi n_r = 0$$

and conserves the zero-order Hamiltonian,

$$H_0(I,\ J) + 2\pi W = 0 \tag{113}$$

we can relate $\Delta\bar{J}$ to ΔI or ΔJ. In particular we wish to examine the neighborhood of the "resonance turning;" i.e., near $d\bar{J}/dI = 0$ for the resonance (see Fig. 9); this turning lies just above the adiabatic barrier and leads to the strongest diffusion in $E_\perp$. Near the turning point, $\Delta J \approx 0$ and, using equations (C1), (C7) and (45), we find

$$\Delta I \approx [sn_r - r(n_s+1)]\Delta\bar{J}\ . \tag{114}$$

From the definition of the normalized perpendicular energy, $E_\perp = u^2 = \sigma(I-J)$, we obtain, for $\Delta J \approx 0$,

$$\Delta E_\perp = \sigma\Delta I$$

so that (114) becomes

$$\Delta E_\perp = \frac{r}{s}(n_s+1) - n_r = \beta\Delta\bar{J}. \tag{115}$$

Substituting (115) in (112) we obtain

$$<\Delta E_\perp^2> = \frac{\tilde{\omega}_\phi}{2\pi}\left(\frac{F_2A_2}{\tilde{\omega}_\phi}\right)^2 \tag{116a}$$

which gives the characteristic time for Arnold diffusion,

$$\tau_{\perp A} = \frac{E_\perp^2}{<(\Delta E_\perp)^2>}\frac{\tau_b}{2} \tag{116b}$$

where τ_b is the bounce period. The diffusion proceeds along all resonances, but at the fastest rate for those resonances that are relatively evenly interspersed.

As an example consider STM parameters with M = 2100. Evaluating $E_\perp$ on the resonance curve at the resonance turning we have

$$E_\perp^{1/2} = \frac{M(\frac{r}{s} - \frac{1}{3})}{2\pi n_r} \tag{117}$$

We also calculate the barrier energy near J = 0 to obtain

$$E_{\perp b} = P_{\perp b} \approx 1.5(\frac{M}{2})^{3/4} \approx 267$$

(The factor of 1.5 is a nominal increase in the barrier due to taking two resonances) For this barrier energy all resonances above

$$2\pi n_s = \frac{M}{P_B^{1/2}} = 122$$

or $n_s \geqslant 20$, lie below the barrier in the stochastic sea. We find groups of resonances that satisfy the interspersal condition near $n_s = 18$ ($n_r = 21$) $n_s = 11$ ($n_r = 13$), etc. However, from the resonance diagram in Fig. 8 and the stochasticity limit in Fig. 11, it is clear that each successively lower interspersal set is farther out in $E_{||}$ and the value of $E_\perp$ where the resonance leaves the stochastic sea is lower. We therefore estimate the Arnold diffusion rate from the nearest or highest n_s resonance $n_s = 18$. Using a maximum value of $\tilde{\omega}_\phi = 1$ and substituting $F_2 \approx E_\perp^{1/6}$ (see Eq. 80) into (116a) then for $E_\perp = 143$ from (117), we find the minimum number of mapping periods to diffuse a characteristic energy interval $E_\perp$ to be $E_\perp^2/<\Delta E_\perp^2> = 7\times10^4$. With $\tau_b \approx 3\times10^{-8}$ sec for STM, we substitute into (116b) to obtain a minimum energy diffusion time along a resonance, $\tau_{\perp A} \approx 0.002$ seconds.

This number can be compared with the characteristic energy diffusion time due to the phase randomization which accompanies collisional pitch-angle scattering. Applying, for example, the treatments of Chirikov[17] and Cohen and Rowlands[18] we estimate a diffusion time (see App. E and for more detail Ref. 12)

$$\tau_{\perp c} = (E_{\perp}/4E_{\parallel})K^{-1/2}(\rho^{-1}-\frac{1}{2})^{-2}\,\tau_c \tag{118}$$

where K is the Chirikov stochasticity parameter defined in (28) and τ_c is the angular scattering collision time. Thus, just above the stochasticity boundary (K $\approx$ 1) the energy diffusion time is of the same order of magnitude as the pitch angle scattering time. For STM parameters, with $\rho = \frac{1}{2}$, evaluating $E_{\perp}$ and $E_{\parallel}$ at the resonance turning with $n_r = 21$, as in the Arnold diffusion case, we find $E_{\perp}/E_{\parallel} = 6$. When substituted into (118) this gives

$$\tau_{\perp c} \approx \frac{2}{3}\tau_c,$$

with $\tau_c \approx .03$ sec (for E $\approx$ 10keV and $n=10^{12}cm^{-3}$). This time is somewhat longer than the $\tau_{\perp A}$ calculated from the Arnold diffusion. However, we have found the maximum rate of Arnold diffusion along a single resonance. Over most of the resonance the diffusion will be slower, and is generally much slower. In addition, the total phase space volume near the barrier is much larger than the phase space volume of the resonance layers in which we expect the Arnold diffusion to be large. Thus, for this particular example we would not expect Arnold diffusion to play a major role in enhancing the collisional heating beyond the adiabatic barrier. For other devices, for which the adiabatic energy is higher and/or the particle density is lower, so that the collisional diffusion times are significantly longer, Arnold diffusion may play a significant role in plasma heating.

IX. Conclusions

A model for two-frequency electron cyclotron resonance heating has been studied, using a mapping approximation. It is shown that, owing to the spatial separation of the resonance zones, the two frequency mapping is four dimensional, rather than two dimensional as with a single frequency. Two important consequences of using two frequencies can, however, be obtained from a two-dimensional approximation to the four-dimensional map These are (1) an increase in the range of energy over which heating can occur, due to the raising of the adiabatic barrier limiting the heating from below; and (2) optimization of this increase by uniformly interspersing the resonances corresponding to the two applied frequencies.

In addition to these processes, there are a number of other effects that arise solely because of the higher dimensionality of the mapping. These effects are associated with Arnold diffusion, in which diffusion occurs along as well as across overlapping resonance layers. In the main heating region this leads to diffusion in parallel energy as well as the lowest order diffusion in perpendicular energy. Arnold diffusion also allows penetration into the region of phase space in which the motion is primarily regular by diffusion along narrow stochastic layers in the neighborhood of the resonances. For real ECRH devices, the first effect leads to enhanced diffusion into the loss cone, while the second results in diffusion to higher energies than predicted from the two dimensional model.

In a real device, collisional effects also cause particles to diffuse into the loss cone and to increase the energy of some particles beyond the adiabatic barrier. For the STM device, in which two frequency heating has been employed, it is found that intrinsic diffusion of the parallel energy can significantly enhance diffusion into the loss cone. The increase in perpendicular energy due to Arnold diffusion is at most comparable to that produced by collisional effects. However, for an appropriate choice of parameters (high barrier energy, high electric fields, and low plasma density) the increase in energy from Arnold diffusion can exceed that due to collisions.

The inclusion of the real electron cyclotron resonance heating dynamics gives rise to an Airy function coefficient for the kick in perpendicular energy when traversing a resonance. Zeros of the Airy function arise from destructive interference of the heating for some particles traversing the resonance twice. These zeros act as a barrier to heating for a single frequency. Due to the higher dimensionality of the phase space, the Airy function zeros cease to be a barrier for two frequency heating. However, even with a single frequency the size of an individual energy kick may be sufficient to jump over an Airy function zero over most of the stochastic phase space.

In addition to the results obtained for experiments, the heating model is useful for studying the dynamics of four-dimensional maps. Arnold diffusion has been studied in simpler problems, but even the simplified dynamics developed in Sec. II allows for a richer set of dynamical processes. The three-resonance theory of Arnold diffusion has also been compared with the numerical values of diffusion obtained from the mapping, shedding light on the applicability of the theory. Some interesting results have been the following. We have shown numerically that higher order fixed points exist on resonances of a single frequency, in addition to the sparse set of lowest order fixed points that exist at the intersections of the two sets of resonance curves. The stability of the fixed points has been analyzed by applying a recently developed theory for four-dimensional symplectic matrices, and the results confirmed numerically. The widths of the resonances are calculated from an averaged Hamilitonian in the neighborhood of a resonance and found to agree with numerical calculations. Reconnection of the islands existing on two branches of a single resonance is found to take place near a turning point of the resonance in action space. It is shown that the reconnection can be predicted from an analytic model.

The adiabatic barrier to heating from below is found by numerically iterating the mapping and shown to correspond, except in regions near resonance turning points, where reconnection occurs, to the "two-thirds rule" for resonance overlap. Diffusion in the thick stochastic layer is shown to be quasi-linear in both actions in regions for which the phase associated with one of the actions is randomized in each mapping period. This result is consistent with the analytic diffusion calculation. The computed rate of Arnold diffusion along a stochastic resonance layer just above the main stochastic sea compares reasonably well with the three resonance theory.

We gratefully acknowledge the assistance of S. M. Hohs in performing the numerical calculations. This research was supported by the Department of Energy Contract DE-ATOE-76ET53059 and the Office of Naval Research Contract NOO014-79-C-0674.

Appendix A. Details of Linear Stability Calculation

The linearization of the mapping (24) is

$$\mathbf{L} = \begin{pmatrix} \frac{\partial I'}{\partial I} & \frac{\partial I'}{\partial J} & \frac{\partial I'}{\partial \phi} & \frac{\partial I'}{\partial \chi} \\ \frac{\partial J'}{\partial I} & \frac{\partial J'}{\partial J} & \frac{\partial J'}{\partial \phi} & \frac{\partial J'}{\partial \chi} \\ \frac{\partial \phi'}{\partial I} & \frac{\partial \phi'}{\partial J} & \frac{\partial \phi'}{\partial \phi} & \frac{\partial \phi'}{\partial \chi} \\ \frac{\partial \chi'}{\partial I} & \frac{\partial \chi'}{\partial J} & \frac{\partial \chi'}{\partial \phi} & \frac{\partial \chi'}{\partial \chi} \end{pmatrix} \tag{A1}$$

with characteristic polynomial

$$F(\Lambda) = \det(\mathbf{L} - \Lambda \mathbf{I}) = 0. \tag{A2}$$

Since $[I',\phi'] = [J',\chi'] = 1$, the mapping (24) and therefore the matrix **L** are symplectic. By the symplectic eigenvalue theorem, if Λ is an eigenvalue, then $1/\Lambda$ is also. Further, by the reality of **L** we know that complex eigenvalues occur in conjugate pairs. Thus, there are just three possible cases:

Case 1: four real roots

$$(\Lambda_{r1},\ 1/\Lambda_{r1},\ \Lambda_{r2},\ 1/\Lambda_{r2})$$

This case is always unstable unless $\Lambda_{r1} = \Lambda_{r2} = 1$ (neutral stability)

Case 2: two real, two complex roots

$$(\Lambda_c, \Lambda_c^*, \Lambda_r, 1/\Lambda_r)$$

Since $\Lambda_c^* = 1/\Lambda_c$, $|\Lambda_c|^2 = 1$.

Case 3: four complex roots

$$(\Lambda_{c1},\ \Lambda_{c1}^*,\ \Lambda_{c2},\ \Lambda_{c2}^*)$$

Here there are two sub-cases:

(a) $\Lambda_{c1}^{*} = \frac{1}{\Lambda_{c1}}, \quad \Lambda_{c2}^{*} = \frac{1}{\Lambda_{c2}}.$

Thus, $|\Lambda_{c1}|^2 = |\Lambda_{c2}|^2 = 1$ and the motion is *stable.*

(b) $\Lambda_{c2} = \frac{1}{\Lambda_{c1}}, \quad \Lambda_{c2}^{*} = \frac{1}{\Lambda_{c1}^{*}}$

Thus, $|\Lambda_{c1}|^2 \neq 1, \quad |\Lambda_{c2}|^2 \neq 1$ and the motion is *unstable.*

Of course, in all cases $\Lambda_1 \Lambda_2 \Lambda_3 \Lambda_4 = 1$, since $F(0) = 1$.

The stability limits of the general 4 x 4 symplectic matrix have been derived by Mackay[14] whose results may be summarized briefly as follows. Owing to the symplectic property, the polynomial (A2) has the reflexive form

$$\Lambda^4 - P\Lambda^3 + Q\Lambda^2 - P\Lambda + 1 = 0 \tag{A3}$$

where P and Q have the well-known equivalents,

$$P = Tr\mathbf{L} \tag{A4}$$

$$Q = \frac{1}{2}[(Tr\mathbf{L})^2 - Tr(\mathbf{L}^2)].$$

Defining $\rho_i = \Lambda_i + \Lambda_i^{-1}$, it easily follows that $P = \rho_1 + \rho_2$ and $Q = \rho_1\rho_2 + 2$, from which Mackay obtains the universal stability diagram illustrated in Fig. 17. The various transitions among eigenvalue configurations are indicated by the inserts showing the local complex Λ-plane.

1. A complex conjugate pair of roots moves to the positive real axis when

$$Q < 2P - 2. \tag{A5}$$

2. A pair moves to the negative real axis when

$$Q < -2P - 2. \tag{A6}$$

3. A non-conjugate pair merges and moves off the unit circle (Krein collision) when

$$Q > 2 + \frac{1}{4}P^2. \tag{A7}$$

4. Since the straight lines (A5) and (A6) are tangent to the parabola (A7) at $P = \pm 4$, we also

require

$$|P| < 4 \tag{A8}$$

for stability.

Note that when $P = \pm 4, Q = 6$, all four roots have merged.

Working out the elements of L, we find, after some lengthy algebra,

$$L = \begin{bmatrix} 1 & 0 & s^2(\alpha+\lambda\beta) & s\beta \\ 0 & 1 & s\beta & \beta/\lambda \\ \sigma^2(A-B) & \sigma^2 B & 1+\alpha(A-B)+\beta(\lambda A-B) & \sigma\frac{\beta}{\lambda}(\lambda A-B) \\ \sigma^2 B & -\sigma^2(A+B) & \alpha B+\beta(B-\sigma A) & 1+\sigma\frac{\beta}{\lambda}(B-\sigma A) \end{bmatrix} \tag{A9}$$

where

$$A = \frac{M}{u^3} \quad B = \frac{3\sigma MJ}{4u^5} \tag{A10}$$

$$\alpha = \frac{1}{N}\cos(s\phi) \qquad \beta = \frac{\lambda\epsilon}{N}\cos(r\phi+\chi) \tag{A11}$$

A typical root locus is shown in Fig. 18 for $\sigma = 1/4$, M = 50, (m,n) = (0,1). Since J = 0, the angular fixed point is $(\phi,\chi) = (45°, 135°)$. For $\epsilon = A_2/A_1 = 0$ all four eigenvalues lie on the unit circle, with one degenerate pair at $\Lambda = 1$. As ϵ is increased, the merged pair at $\Lambda = 1$ split and move along the unit circle, colliding with the other pair when $\epsilon = 4/9$. After this "Krein collision," each collidee moves off the unit circle, as shown. At $\epsilon = 1$, pairs of roots again collide and move onto the real axis ever after. Calculating root loci for a number of m-values, we find that the ϵ - M plane is subdivided as shown in Fig. 6. For $M \lesssim 17.0$, there are no stable fixed points. For $17 \lesssim M \lesssim 44.5$, there is a stability window between the upper curve and the line $\epsilon_1 = 4/9$. For $M \gtrsim 44.5$, the $(\phi,\chi) = (45°, 135°)$ fixed point is stable for $0 < \epsilon < 4/9$. It is remarkable that the critical value $\epsilon = 4/9$ is independent of M, and even more remarkable that the second value, $\epsilon = 1$, is independent of both M and σ! The simplicity of these initial numerical incursions into what seemed impassable mathematical territory led us to attempt an analytic solution, which was greatly facilitated by the theory of

Mackay. We are indebted to him for making his preliminary results available to us.

After successfully applying their theory to the J = 0 case, we found a second region of stability for $\epsilon \geqslant 1$ and $(\phi,\chi) = (0,180°)$ as shown in Fig. 6. There are apparently no stable fixed points at all for $\frac{4}{9} < \epsilon < 1$. For $J \neq 0$, for which we have no theoretical results, a typical $\epsilon - M$ plot (Fig. 7) shows a stability window for $\epsilon < 1$ and $(\phi,\chi) = (0,180°)$ with no stable fixed points for $\epsilon > 1$.

Analytic Results for J = 0 Fixed Points.

Setting B = 0 in L we find,

$$P = 4 + \frac{A}{N}[\sigma_1 + \sigma_2\epsilon(\lambda+\sigma)] \tag{A12}$$

$$Q = 6 + \frac{2A}{N}[\sigma_1 + \sigma_2\epsilon(\lambda+\sigma)] - \sigma_1\sigma_2\sigma^2\epsilon(\frac{A}{N})^2,$$

where $\sigma_1 = \cos(s\phi)$ and $\sigma_2 = \cos(r\phi+\chi)$ are ± 1 according to Eqs. (34) and (35).

First consider condition (A5), which for stability becomes

$$-\sigma_1\sigma_2\left(\frac{\sigma^2\epsilon A^2}{N^2}\right) > 0. \tag{A13}$$

This excludes the cases $\sigma_1 = \sigma_2$, so that the combinations $(\phi,\chi) = (0,0)$ and $(\sigma\pi,-\sigma\pi)$ are never stable. Thus, we may rewrite (A12) as

$$P = 4 + \frac{\sigma_1 A}{N}[1-\epsilon(\lambda+\sigma)] \tag{A14}$$

$$Q = 6 + \frac{2\sigma_1 A}{N}[1-\epsilon(\lambda+\sigma)] + \sigma^2\epsilon(\frac{A}{N})^2.$$

Next we consider the limit $Q = 2 + P^2/4$. Substituting (A14) in this equation yields a quadratic in ϵ,

$$(2\sigma+1)^2\epsilon^2 - [(2\sigma+1)^2 + 1]\epsilon + 1 = 0, \tag{A15}$$

whose solutions are

$$\epsilon_1 = (2\sigma+1)^{-2} \qquad \text{(A16)}$$
$$\epsilon_2 = 1,$$

independent of M and valid for both $\sigma_1\sigma_2 = -1$ cases. For $\sigma = 1/4$, this gives $\epsilon_1 = 4/9$, as observed in Fig. 6.

So far we have proven that the motion is unstable for $\epsilon_1 < \epsilon < \epsilon_2$, with possible stability outside these limits. To explore the outer limits, consider the third limit, $Q + 2 = -2P$, which gives a quadratic in A/N,

$$\sigma^2\epsilon(\frac{A}{N})^2 + 4\sigma_1[1-\epsilon(\lambda+\sigma)]\frac{A}{N} + 16 = 0, \qquad \text{(A17)}$$

with solution

$$\frac{1}{2}\,\sigma^2\epsilon(\frac{A}{N}) = -\sigma_1[1-\epsilon(\lambda+\sigma)] \pm \sqrt{[1-\epsilon(\lambda+\sigma)]^2-4\sigma^2\epsilon}. \qquad \text{(A18)}$$

For fixed σ, this equation yields a stability limit $M = M(\epsilon)$ via

$$M = \frac{1}{\sqrt{2A}}\left(\frac{2\pi}{\sigma}\right)^{3/2.} \qquad \text{(A19)}$$

Together with the critical values (A16), the solutions (A18) map the PQ plane into the ϵ-M plane depicted in Fig. 6.

For $\sigma_1 = -1$, i.e., $(\phi,\chi) = (45°\ ,\ 135°\ )$, Eq. (A18) has two real branches for $\epsilon < \epsilon_1 = (\sigma+\lambda)^{-2}$, as shown in Fig. 6 for $\sigma = 1/4$. Setting the discriminant equal to zero, we recover the quadratic (A15), showing that at ϵ_1 there is a critical value $A = 4N(\sigma+\lambda)/\sigma$, or

$$M_1^2 = \frac{(n\pi)^3(\sigma+\lambda)}{\sigma^2\sqrt{(\lambda+\sigma)^4+\lambda^2}} \qquad \text{(A20)}$$

For $\sigma = \frac{1}{4}$ and n = 1 this yields $M_1 = 17.00$, as indicated in Fig. 6, corresponding to point b in Fig. 17.

Letting $\epsilon \rightarrow 0$ in (A17) we find $A \rightarrow 4$ on the upper branch, giving a second critical value

$$M_2 = (\pi/n\sigma)^{3/2}. \tag{A21}$$

For $\sigma = \frac{1}{4}$ and n = 1, this gives $M_2 = 44.5$, as observed in Fig. 6. (P = 0, Q = -2 in Fig. 17).

When $M < M_1$ there are no stable period-one fixed points for any ϵ. This corresponds to a locus in the PQ plane initially below the line Q = 2 - 2P and crossing this line to the left of P = -4, so that it never enters the stable arrowhead. For $M_1 < M < M_2$ the motion is unstable for $\epsilon = 0$ but has a stable window, going unstable again at ϵ_1. This corresponds to a PQ locus crossing $Q=2-2P$ to the right of P = -4. (Root locus of Fig. 18) For $M > M_2$ the motion is stable for all $\epsilon < \epsilon_1$, the P-Q locus lying initially within the stable region.

For $\sigma_1 = +1(\phi = 0, \chi = 180°)$ the stability picture is quite different. Since P > 4 for $\epsilon << 1$, stable motion is possible only when ϵ exceeds a critical value, evidently $\epsilon_1 = (\lambda+\sigma)^{-2}$, as we know from (16) that the motion is unstable for $\epsilon_1 < \epsilon < 1$. In the P-Q plane, the locus for constant M begins in the right wedge region for $\epsilon = 0$, crosses the parabola at ϵ_1 and again at $\epsilon = 1$, entering the stable region if $P > -4$ at $\epsilon = 1$. From (14) this requires $A > 4N/\sigma$, or $M > M_3$, where

$$M_3^2 = \frac{(n\pi)^3}{\sigma^2(1+\lambda^2)^{1/2}}. \tag{A22}$$

As ϵ is increased further, the motion again goes unstable upon crossing the line Q + 2 = -2P. Solving (A17) with $\sigma_1 = +1$ gives

$$\frac{1}{2}\sigma^2\epsilon(\frac{A}{N}) = \epsilon(\lambda+\sigma) - 1 \pm ([\epsilon(\lambda+\sigma)-1]^2 - 4\sigma^2\epsilon)^{1/2}, \tag{A23}$$

with M(ϵ) given by (A19). For fixed M, the critical value of ϵ is of course directly given by (A17). Equation (A23) is useful for calculating the limiting values of M as $\epsilon \rightarrow \infty$. The results are $A_+ \rightarrow \infty$, for which $M \rightarrow 0$, and $A_- \rightarrow 4\lambda/(\lambda+\sigma)$, which yields

$$M_4^2 = \left(\frac{\lambda+\sigma}{\lambda}\right)\left(\frac{n\pi}{\sigma}\right)^3 \tag{A24}$$

The two branches of (A23) are plotted in Fig. 6 for $\sigma = \frac{1}{4}$, for which the limiting values are $M_3 = 17.60$ and $M_4 = 48.80$, in complete agreement with a numerical eigenvalue calculation. The various transitions in the eigenvalue configurations are indicated on the figure.

In conclusion, we have been able to give a surprisingly complete account of linear stability for the J = 0 fixed points. In addition, we have obtained a detailed description of the configuration of eigenvalues for varying M, σ and ϵ, which may have a bearing on the rather slow divergence rates observed in many cases. Typically, as the amplitude ratio ϵ is increased, stable motion occurs for $(\phi,\chi) = (\sigma\pi, (1-\sigma)\pi)$ at low ϵ, followed by an unstable hiatus with no stable fixed points. A second stable region exists for $(\phi,\chi) = (0,\pi)$ for $\epsilon > 1$, as the r-fold symmetry dominates.

What happens for the $J \neq 0$ fixed points? In this case many more terms survive in the expressions for P and Q, especially in $Tr(\mathrm{L}^2)$, making an analytic solution much more difficult. A numerical search suggests that, in contrast to the J = 0 cases, the $\phi = 0, \chi = 180°$ fixed point is always stable for $\epsilon < 1$, as shown in Fig. 7 for (m,n) = (1,1). So far we have found no stable fixed points for $\epsilon > 1$.

Appendix B. Resonance Width Computation

The principal resonances are

$$\Delta\Psi = -2\pi n_s \tag{B1}$$

$$\lambda\Delta\Psi + \Delta\chi = -2\pi n_r \tag{B2}$$

where

$$\Delta\Psi = \frac{M}{2u^3}(2P-3\sigma J) \tag{B3}$$

$$\Delta\Psi = -\frac{\sigma^2 MJ}{2u^3} \tag{B4}$$

and

$$u^2 = P-\sigma J \ . \tag{B5}$$

Equations (B1-B2) are nonlinear functions of P and J, which may be solved using u as a parameter. Typical resonance curves for various n_s and n_r are illustrated in Fig. 8. Our task here is to calculate the libration amplitude about these resonances.

B.1 S-Fold Resonances

Near an s-fold resonance (B1) the motion is described by the averaged Hamiltonian

$$H = H_0(P,J) + \frac{1}{N}\cos(\Psi + 2\pi m n_s) \tag{B6}$$

where m is integer time and

$$H_0(P,J) = -\frac{M}{u}(2P-\sigma J). \tag{B7}$$

Using the generating function

$$F(\tilde{P},\Psi,\tilde{J},\chi) = \tilde{P}(\Psi + 2\pi m n_s) + \tilde{J}\chi \tag{B8}$$

Eq. (B6) becomes

$$\tilde{H} = H_0(P,J) + 2\pi n_s P + \frac{1}{N}\cos\tilde{\Psi}, \tag{B9}$$

where $\tilde{\Psi} = \Psi + 2\pi m n_s$.

The customary method for calculating the resonance width is to Taylor expand about P_r to obtain a pendulum Hamiltonian. This gives

$$\Delta P_{\max} = \left(\frac{2}{NG}\right)^{\frac{1}{2}} \tag{B10}$$

where

$$G = \frac{\partial^2 H_0}{\partial J^2} = \frac{M}{4u^5}(2P - 5\sigma J) \quad . \tag{B11}$$

Since $P \rightarrow 5\sigma J/2$ as $J \rightarrow J_{\max}$, we see that $\Delta P_{\max}$ diverges there. The physical reason for the failure of the quadratic approximation to $H(P,J)$ is that the resonances corresponding to the upper and lower branches of a resonance curve interact strongly near $J_{\max}$. Adding cubic terms to the expansion does not help because the two expansions do not match up in the reconnection region.

To correctly describe this rather complex interaction we write the two-dimensional reduced map corresponding to (B9) in the form

$$P' = P + \frac{1}{N}\cos\Psi \tag{B12}$$
$$\Psi' = \Psi + f(P'),$$

where $f(P) = \partial H_0/\partial P$ and we have dropped the tilde on Ψ. The fixed points of (B12) are just the resonances (B1), which may be written

$$f(P) + 2\pi n_s = 0. \tag{B13}$$

Using (B3) and (B5) this becomes a cubic in u;

$$u^3 - u_0 u^2 + \frac{1}{2} u_0 \sigma J = 0 \tag{B14}$$

where $u_0 = M/2\pi n_s$ is the velocity when $J = 0$. From (B14) is follows that J attains its maximum value $\sigma J^* = 8u_0^2/27$ when $u^* = 2u_0/3$, and that the maxima lie along the line $P = 5\sigma J/2$ (Fig. 19).

The fact that $f'(P) = 0$ between the two branches of the resonance curve has profound effects on the form and stability properties of the corresponding island chains of the mapping (B12). From the theory of Howard and Hohs[15] such mappings have the following general properties:

1 Corresponding to each of the roots of $f(P) + 2\pi n_s = 0$ there exists an island chain at $P_i, i=1,2,\ldots,k$.

2 Let $f = f(P;\vec{\alpha})$, where $\vec{\alpha}$ is a set of parameters. Then if $f' = \partial f/\partial P$ vanishes for some $\vec{\alpha}^*$, two island chains merge at P^* given by $f(P^*,\vec{\alpha}^*) = -2\pi n_s$.

3 Prior to merging, the (period-one) island centers are shifted in phase by 180 degrees. Reconnection occurs at $\vec{\alpha}_r$ given by

$$\int_{P_1(\vec{\alpha})}^{P_2(\vec{\alpha})} [f(P,\vec{\alpha}) + 2\pi n_s]\, dP = \frac{2}{N} \quad . \tag{B15}$$

Figure 20 depicts the Hamiltonian level curves before and after reconnection for the mapping (B12). For the lower separatrix, with x-point at (P_1,π) , Eq. (B9) gives

$$\frac{M}{u_1}(2P_1 - \sigma J) - \frac{M}{u}(2P - \sigma J) + 2\pi n_s (P - P_1) + \frac{2}{N}\cos^2\frac{\Psi}{2} = 0. \tag{B16}$$

To obtain the amplitude, we set $\Psi = 0$ before reconnection and $\Psi = \pi$ afterwards. Note that this gives the *upper* island width after reconnection. Defining $\delta = \cos^2\Psi/2$ and using (B5) to eliminate P and (B14) to eliminate J gives

$$u^3 - 2u_0 u^2 + [\frac{2u_0\delta}{MN} + u_1(4u_0 - 3u_1)]u - 2u_1^2(u_0 - u_1) = 0, \tag{B17}$$

This equation is easily solved numerically with $\delta = 1$.

After reconnection, with $\delta=0$, (B17) factors into

$$(u-u_1)^2(u-u_3) = 0 \tag{B18}$$

where $u_3 = 2(u_0-u_1)$. The two upper half-widths are then P_3-P_2 and P_2-P_1, with P given by (B5). The width of the upper island chain before reconnection is found by setting $\delta = -1$ in (B17). Figure 9 shows a set of resonance curves and widths for $M=100, \sigma=1/4$ and $\epsilon=1$. Note that the widths go to zero when $J \rightarrow J_{max}$, when the loops in Fig. 20 become cusps.

B.2 R-Fold Resonances

The averaged Hamiltonian near an r-fold resonance is

$$H = H_0(P,J) + \frac{\epsilon}{N}\cos(\lambda\Psi+\chi+2\pi n_r m). \tag{B19}$$

Using the generating function

$$F(\bar{P},\tilde{J}_0\Psi,\chi) = \bar{P}(\lambda\Psi+\chi+2\pi n_r m) + \tilde{J}\chi \tag{B20}$$

gives $P=\lambda\bar{P}$ and $J=\bar{P}+\tilde{J}$, so that

$$\bar{H} = H_0(\lambda\bar{P},\ \bar{P}+\tilde{J}) + 2\pi n_r\bar{P} + \frac{\epsilon}{N}\cos\Psi. \tag{B21}$$

Thus

$$\tilde{J} = J - P/\lambda \tag{B22}$$

is a constant of the motion. That is, libration occurs along a line of slope λ in the $P-J$ plane.

Using (B22) in (B5) gives $u^2 = P-\sigma J = \bar{P}-\sigma\tilde{J}$, so that the resonance condition (B2) becomes

$$u^3 - u_{0r}u^2 + \frac{\sigma}{2\lambda}u_{0r}J = 0 \tag{B23}$$

where $u_{0r} = \lambda M/2\pi n_r$. In the new coordinates this becomes

$$u^3 - \bar{u}_0u^2 + (\frac{\lambda}{\lambda+1})\bar{u}_0\sigma\tilde{J} = 0 \ . \tag{B24}$$

Equations (B23) and (B24) may be used to generate r-fold resonance curves in the $P-J$ plane and $\tilde{P}-\tilde{J}$ plane, respectively. It is easily seen that the maxima occur in the $P-J$ plane when $u^*=(2/3)u_{0r}$, along the line

$$P^* = (1+\frac{3}{2\lambda})\sigma J^* \quad . \tag{B25}$$

The new Hamiltonian (B21) may be written

$$\tilde{H} = -\frac{M}{u}(\lambda+1)\tilde{P} + \frac{\lambda M}{u_{0r}}\tilde{P} + \frac{M\sigma\tilde{J}}{u} + \frac{\epsilon}{N}\cos\tilde{\Psi} = 0 \quad . \tag{B26}$$

Again taking $\tilde{P}=\tilde{P}_1$, and $\tilde{\Psi}=0$ for the lower separatrix gives

$$\frac{M}{u_1}[(\lambda+1)\tilde{P}_1-\sigma\tilde{J}] - \frac{M}{u}[(\lambda+1)\tilde{P} - \sigma\tilde{J}] + \frac{\lambda M}{u_{0r}}(u^2-u_1^2) + \frac{2\epsilon}{N}\cos^2\frac{\tilde{\Psi}}{2} = 0 \quad . \tag{B27}$$

After some manipulation, this becomes

$$u^3 - 2\tilde{u}_0u^2 + [\frac{4\epsilon\delta\tilde{u}_0}{(\lambda+1)MN} + u_1(4\tilde{u}_0-3u_1)]u - 2u_1^2(\tilde{u}_0-u_1) = 0 \tag{B28}$$

which is exactly (B17), with u_0 replaced by $\tilde{u}_0$ and M by $\frac{1}{2}(\lambda+1)M$. After reconnection, with $\delta=0$, (B28) factors into (B18) with $u_3=2(\tilde{u}_0-u_1)$. The rest of the calculation proceeds as for the s-fold resonances. Finally, we transform back to (P,J) to obtain the set of r-fold curves shown in Fig. 10.

Appendix C. Calculation of Arnold Diffusion

Here we determine the thin layer Arnold diffusion rate in the guiding resonance (59) using the three resonance, stochastic pump model[12]. Including the two guiding resonances (60) and (61), we have the three resonance Hamiltonian

$$H = H_0(I,J) + F_0 \cos(r\phi + \chi + 2\pi n_r n) + F_1\cos(s\phi + 2\pi(n_s+1)n) + F_2 \cos(s\phi + 2\pi n_s n)$$

where n is the (integer) time and

$$\begin{aligned} H_0 &= -\frac{M\sigma}{u}(2I-J) \\ F_0 &= \epsilon(1+\epsilon^2\lambda^2)^{-1/2} \qquad \text{(C1)} \\ F_1 &= F_2 = (1+\epsilon^2\lambda^2)^{-1/2} \end{aligned}$$

are respectively the amplitudes of the guiding resonance, the stochastic pump driving resonance and the Arnold diffusion driving resonance. We introduce the new action $W = -H/2\pi$ and its canonical angle $\theta = 2\pi n$ and work in an extended phase space. The new Hamiltonian is

$$\begin{aligned} H_e = H_0(I,J) + 2\pi W + F_0 \cos(r\phi+\chi+n_r\theta) \qquad \text{(C2)} \\ + F_1\cos(s\phi+n_s\theta+\theta) + F_2\cos(s\phi+n_s\theta). \end{aligned}$$

To expose the transformed action $\bar{J}$ that is conserved in the absence of Arnold diffusion, we transform (C2) using the generating function

$$S = \bar{I}(r\phi+\chi+n_r\theta) + \bar{J}\chi + \bar{W}(\beta\theta-\chi), \qquad \text{(C3)}$$

where

$$\beta = \lambda(n_s+1) - n_r. \qquad \text{(C4)}$$

This yields the new Hamiltonian

$$\begin{aligned} \bar{H} = \bar{H}_0 + F_0 \cos\bar{\phi} + F_1 \cos[\lambda^{-1}(\bar{\phi}+\bar{\beta})] \qquad \text{(C5)} \\ + F_2\cos[\lambda^{-1}\bar{\phi}+(\lambda^{-1}-\beta^{-1})\bar{\theta} - \beta^{-1}\bar{\chi}] \end{aligned}$$

where $\bar{H}_0 = H_0(r\bar{I},\bar{I}-\bar{W}+\bar{J}) + 2\pi n_r\bar{I} + 2\pi\beta\bar{W}$,

$$
\begin{aligned}
I &= r\overline{I} \\
J &= \overline{I} - \overline{W} + \overline{J} \\
W &= n_r\overline{I} + \beta\overline{W} \quad .
\end{aligned}
\tag{C6}
$$

In the absence of the Arnold diffusion driving resonance $(F_2 = 0)$, $\overline{H}$ is independent of $\overline{\chi}$ and therefore $\overline{J}$ is conserved. Inverting (C6),

$$
\overline{J} = J + \frac{sW-(n_s+1)I}{r(n_s+1)-sn_r} = const. \tag{C7}
$$

The remaining motion is approximately that of a periodically driven pendulum. To see this we expand $\overline{H}$ about the resonance values of the actions $\overline{I}_R, \overline{J}_R, \overline{W}_R$, satisfying

$$
\overline{\omega}_\phi = \left(\frac{\partial \overline{H}_0}{\partial \overline{I}}\right)_R = 0 \tag{C8}
$$

to obtain

$$
\overline{H}_0 \approx \overline{H}_0(\overline{I}_R, \overline{J}_R, \overline{W}_R) + \frac{1}{2}G(\Delta\overline{I})^2 \tag{C9}
$$

where

$$
G = \left(\frac{\partial^2 \overline{H}_0}{\partial \overline{I}^2}\right)_R
$$

is the nonlinearity parameter. The term linear in $\Delta\overline{I} = \overline{I} - \overline{I}_R$ vanishes by virtue of (C8). Ignoring the constant term in (C9), we have from (C5)

$$
\Delta\overline{H} = \frac{1}{2}G(\Delta\overline{I})^2 + F_0\cos\overline{\phi} + F_1\cos[\lambda^{-1}(\overline{\phi}+\overline{\theta})]. \tag{C10}
$$

Since $\Delta\overline{H}$ is independent of $\overline{J}$, $\overline{\theta} = \overline{\omega}_\theta n$ where

$$
\overline{\omega}_\theta = \frac{\partial \overline{H}_0}{\partial \overline{W}}. \tag{C11}
$$

Hamiltonian (C10) is that of a periodically perturbed pendulum. The linearized frequency of libration (for small oscillations of the pendulum) is

$$\tilde{\omega}_\phi = (F_0 G)^{1/2}. \tag{C12}$$

Near the separatrix of the pendulum, the driving term F_1 produces the usual stochastic motion within a thin layer surrounding the separatrix. The motion within this stochastic layer is randomized on the time scale $\overline{T}_\phi$ of the mean half-period for the perturbed separatrix motion [12]

$$\overline{T}_\phi = \tilde{\omega}_\phi^{-1} \ln\left|\frac{32e}{w_1}\right| \tag{C13}$$

where w_1 is the relative energy at the stochastic barrier defining the edge of the layer, and e is the natural base.

To determine the Arnold diffusion rate, we re-introduce the F_2 driving term and calculate the change in $\overline{J}$ for an initial condition in the separatrix layer. From (C5), $\dot{\overline{J}} = -\partial\overline{H}/\partial\overline{\chi}$ and

$$\Delta\overline{J} = -F_2\beta^{-1}\int_{-\infty}^{\infty} dn \, \sin[\lambda^{-1}\overline{\phi}(\tilde{\omega}_\phi n) + \overline{\omega}_d n + \chi_0] \tag{C14}$$

where

$$\overline{\phi}(\xi) = 4\tan^{-1}(e^\xi) - \pi \tag{C15}$$

is the phase variation of the unperturbed separatrix motion of the pendulum,

$$\overline{\omega}_d = (\lambda^{-1} - \beta^{-1})\overline{\omega}_\theta - \beta^{-1}\overline{\omega}_\chi \tag{C16}$$

is the effective driving frequency, with

$$\overline{\omega}_\chi = \left(\frac{\partial\overline{H}_0}{\partial\overline{J}}\right)_R, \tag{C17}$$

and χ_0 is an initial phase. Changing variables to $\xi = \tilde{\omega}_\phi n$ and expanding the sine function, only its symmetric part contributes to the integral and we find

$$\Delta\overline{J} = -F_2\beta^{-1}\tilde{\omega}_\phi^{-1} \sin\chi_0 \int_{-\infty}^{\infty} d\xi \, \cos[\lambda^{-1}\overline{\phi}(\xi) - Q\xi] \tag{C18}$$

where $Q = -\overline{\omega}_d/\tilde{\omega}_\phi > 0$ is the ratio of the effective driving frequency to the libration frequency of the pendulum. The integral in (C18) is the Melnikov-Arnold integral $A_m(Q)$ with $m = 2\lambda^{-1}$;

$$\Delta\bar{J} = -F_2\beta^{-1}\bar{\omega}_\phi^{-1}\sin\chi_0\, A_m(Q). \tag{C19}$$

Squaring $\Delta\bar{J}$, averaging over χ_0 and dividing by $\bar{T}_\phi$, we obtain the Arnold diffusion coefficient

$$D_A = \frac{(\Delta\bar{J})^2_{\chi_0}}{2\bar{T}_\phi} \frac{1}{4\bar{T}_\phi} F_2^2\beta^{-2}\bar{\omega}_\phi^{-2}A_m^2(Q). \tag{C20}$$

For large Q, A_m has the asymptotic form (see Ref. 12)

$$A_m \sim 4\pi(2Q)^{m-1}\, e^{-\pi Q/2}/(m-1)! \tag{C21}$$

For $\lambda \approx 1$, we require A_2, which has the exact form

$$A_2(Q) = 4\pi Q e^{\pi Q/2}/\sinh(\pi Q). \tag{C22}$$

Appendix D. Loss Cone Boundary Value Problem

As shown in Fig. 14 we seek the solution to the equation

$$\frac{1}{r}\frac{\partial}{\partial r}(r\frac{\partial f}{\partial r}) + \frac{1}{r^2}\frac{\partial^2 f}{\partial \theta^2} = -2\pi\frac{\delta(r-d)\delta(\theta-\theta_1)}{r} \tag{D1}$$

in the wedge $r < r_B, -\theta_0 \leqslant \theta \leqslant \pi/2$, where from (64),

$$\tan\theta_0 = \epsilon. \tag{D2}$$

The boundary conditions are

$$\frac{\partial f}{\partial \theta} = 0 \ at \ \theta = \frac{\pi}{2}, \tag{D3}$$

$$\frac{\partial f}{\partial r} = 0 \ at \ r = r_B, \tag{D4}$$

$$f = 0 \ at \ \theta = \theta_0. \tag{D5}$$

The solution to (D1) which satisfies the boundary conditions is

$$f = \sum_n A_n (\frac{r}{d})^{\alpha_n} \sin\alpha_n(\theta+\theta_0), \qquad r<d \tag{D6}$$

$$= \sum_n B_n \left[(\frac{d}{r})^{\alpha_n} + (\frac{d}{r_B})^{2\alpha_n}(\frac{r}{d})^{\alpha_n} \right] \sin\alpha_n(\theta+\theta_0), \qquad r>d$$

where

$$\alpha_n = \alpha_0 n, \tag{D7}$$

$$\alpha_0 = \left[1 + \frac{2}{\pi}\theta_0\right]^{-1},$$

and the sums are over the odd integers $n = 1, 3, \ldots$. Since f is continuous at $r = d$, we find from (D6) that

$$A_n = B_n\left[1 + (\frac{d}{r_B})^{2\alpha_n}\right]. \tag{D8}$$

The discontinuity in the gradient of f is due to the source on the right hand side of (D1). Multiplying (D1) by $\sin[\alpha_k(\theta+\theta_0)]$ and integrating over the range $-\theta_0<\theta<\pi/2$, we obtain

$$\frac{d}{dr}(r\frac{df}{dr}) - \frac{\alpha_k^2}{r}f = -2\pi\frac{\sin[\alpha_k(\theta_1+\theta_0)]}{\frac{\pi}{4}+\frac{\theta_0}{2}}\delta(r-d),$$

Integrating this over r from $d-$ to $d+$, we obtain

$$B_k = \frac{4}{k}\sin[\alpha_k(\theta_1+\theta_0)]. \tag{D9}$$

Equations (D6) - (D9) give the unique solution to (D1). We are interested in electron cyclotron resonance heating where the source particles are injected at low energies $d<<r_B$. For convenience we also choose $\theta_1 = \pi/2-$; the final results are not sensitive to the choice of injection angle.

For these choices,

$$f = 4\sum_k(-1)^{(k-1)/2}\frac{1}{k}(\frac{r_<}{r_>})^{\alpha_k}\sin[\alpha_k(\theta+\theta_0)] \tag{D10}$$

where the sum is over k odd and

$$r_< = \min(r,d),$$

$$r_> = \max(r,d).$$

To obtain the mean loss rate ν_L and the mean energy E_L of a lost particle, we must find the particle flux S_L, the energy flux P_L and the total number of particles N_T. The differential flux at the loss cone edge is

$$F = D_0\frac{1}{r}\frac{\partial f}{\partial\theta}|_{\theta=-\theta_0}. \tag{D11}$$

We write the total particle flux S_L as

$$S_L = \int_0^{r_0} F_L \frac{r}{r_0} dr + \int_{r_0}^{r_B} F_L\, dr, \tag{D12}$$

where we have assumed $r_0 = x_0 \sec\theta_0 < r_B$ and inserted the factor r/r_0 in view of the discussion following (6.7). For $r_0 > r_B$ the second term in (D12) is omitted. The integrals in (D12) are elementary. Similarly, the power flux P_L is

$$P_L = \Delta \int_0^{r_0} rF_L \frac{r}{r_0} dr + \Delta \int_{r_0}^{r_B} rF_L\, dr \tag{D13}$$

where we have written the total energy per particle at the loss cone edge as $E = r\Delta$, where from (15)

$$\Delta = NA_1 \frac{\delta\omega}{\omega_1} \cos\theta_0. \tag{D14}$$

Finally, the total number of particles in the wedge is given by

$$N_T = \int_{-\theta_0}^{\pi/2} d\theta \int_0^{r_B} rdrf. \tag{D15}$$

For $\alpha_0 < 1$, the dominant ($k = 1$) terms for S_L, P_L and N are

$$\frac{S_L}{4D_0\alpha_0} = \frac{1}{1-\alpha_0}\left(\frac{d}{r_0}\right)^{\alpha_0} + \frac{\delta_K}{\alpha_0}\left[\left(\frac{d}{r_0}\right)^{\alpha_0} - \left(\frac{d}{r_B}\right)^{\alpha_0}\right] \tag{D16}$$

$$\frac{P_L}{4D_0\alpha_0\Delta} = \frac{1}{2-\alpha_0} r_0\left(\frac{d}{r_0}\right)^{\alpha_0} + \frac{\delta_K}{\alpha_0 - 1}\left[r_0\left(\frac{d}{r_0}\right)^{\alpha_0} - r_B\left(\frac{d}{r_B}\right)^{\alpha_0}\right] \tag{D17}$$

$$\frac{N\alpha_0}{4} = \frac{1}{2-\alpha_0} r_B^2 \left(\frac{d}{r_B}\right)^{\alpha_0} . \tag{D18}$$

Here $\delta_K = 1$ for $r_0 < r_B$ and $\delta_K = 0$ for $r_0 < r_B$. Corrections of order d/r_0 and d/r_B have been omitted.

Appendix E. Neoclassical Energy Diffusion

We outline here the derivation of energy diffusion due to phase randomization which accompanies pitch-angle scattering. For single-frequency (ω_1) heating in the presence of pitch-angle scattering, the mapping can be written as

$$E_\perp' = E_\perp + A\sin\Psi - \zeta \tag{E1a}$$

$$E_\parallel' = E_\parallel + \zeta \tag{E1b}$$

$$\Psi' = \Psi + B(E_\perp', E_\parallel') \tag{E1c}$$

where ζ is the (random) change in $E_\parallel$ (or $-E_\perp$) due to collisions in a mapping iteration time $\tau_b/2$, i.e., $<\zeta^2> \approx <(\Delta E_\perp)^2> = m^2 v_\perp^2 \ <(\Delta v_\perp)^2>$. In terms of the angular scattering we have $<\zeta^2> = m^2 v_\perp^2 v_\parallel^2 \ <(\Delta\theta)^2> \approx 2E_\perp E_\parallel \ \tau_b/\tau_c$, where θ is the pitch angle and τ_c is the angular scattering time.

Introducing the total energy E as a new variable, and linearizing (E1c) about $E = E_0, E_\parallel = E_{\parallel 0}$ gives the mapping

$$E' = E + A \ \sin\Psi \tag{E2}$$

$$E_\parallel' = E_\parallel + \zeta$$

$$\Psi' = \Psi + B + \frac{\partial B}{\partial E_\perp}(E' - E_0) + \left(\frac{\partial B}{\partial E_{\parallel 0}} - \frac{\partial B}{\partial E_{\perp 0}}\right)(E_\parallel' - E_{\parallel 0})$$

where $E_{\perp 0} \equiv E_0 - E_{\parallel 0}$.

Defining $p = B_0 + (\partial B/\partial E_\perp)(E - E_0)$, $q = (\frac{\partial B}{\partial E_{\parallel 0}} - \frac{\partial B}{\partial E_{\perp 0}})(E_\parallel - E_{\parallel 0})$, we obtain the system studied by Chirikov[17] and Cohen and Rowlands[18],

$$p' = p + K \ \sin\Psi \tag{E3}$$

$$\Psi' = \Psi + p' + q'$$

$$q' = q + \xi$$

with $K \equiv A\ \partial B/\partial E_\perp$, and $\xi = [(\partial B/\partial E_\parallel) - (\partial B/\partial E_\perp)]\zeta$. The r.m.s. value of ξ is $\sigma^{1/2}$, where

$$\sigma = \left(\frac{\partial B}{\partial E_{\perp 0}} - \frac{\partial B}{\partial E_{\parallel 0}}\right)^2 <\zeta^2> \tag{E4}$$

$$\approx 2\left(\frac{\partial B}{\partial E_{\perp 0}} - \frac{\partial B}{\partial E_{\parallel 0}}\right)^2 E_{\perp 0}E_{\parallel 0}\tau_b/\tau_c \quad .$$

Assuming weak collisionality ($\sigma < 1$), then just above the adiabatic barrier (i.e., where $K \approx 1$), the parameter $S \equiv K^{3/2}\sigma^{-1} > 1$, indicating banana-regime transport[17,18]. Thus the diffusion coefficient for p (with time in units of the mapping time) is[17,18] $D_p \approx \sqrt{K}\,\sigma$. Translating back to the physical variable E and actual time, the corresponding energy diffusion coefficient is

$$D_E \approx 4\sqrt{K}\left(\frac{\partial B}{\partial E_{\perp 0}}\right)^{-2}\left(\frac{\partial B}{\partial E_{\perp 0}} - \frac{\partial B}{\partial E_{\parallel 0}}\right)^2 E_{\perp 0}E_{\parallel 0}/\tau_c \tag{E5}$$

$$\approx 4\sqrt{K}E_{\perp 0}E_{\parallel 0}(\rho^{-1} - 1/2)^2/\tau_c$$

where the second form is obtained using Eq. (9) and the approximation $E_{\parallel 0}/E_{\perp 0} << 1$. In this same approximation, the energy diffusion is essentially $E_\perp$ diffusion.

References

1. R. A. Dandl, A. C. England, W. B. Ard, H. O. Eason, M. C. Becker, and G. M. Haas, Nucl. Fusion 4,344 (1964).

2. N. C. Wyeth, A. J. Lichtenberg and M. A. Lieberman, Plasma Phys. 17,679 (1975).

3. R. A. Dandl, H. O. Eason, G. G. Guest, C. L. Hedrick, H. Ikegami, and D. B. Nelson, in Plasma Physics and Controlled Fusion IAEA, Vol. II p. 141 (1975).

4. B. G. Logan, Comments on Plasma Phys. and Controlled Fusion 6,199 (1981).

5. F. Jaeger, A. J. Lichtenberg, and M. A. Lieberman, Plasma Phys. 14,1073 (1972); M. A. Lieberman and A. J. Lichtenberg, Plasma Phys. 15,125 (1973).

6. A. F. Kuckes, Plasma Phys. 10,367 (1968); H. Grawe, Plasma Phys. 11 151 (1969); J. C. Sprott, Phys. Fluids 14,2703 (1971).

7. N. Lazar, J. Barter, R. Dandl, W. Vergilio, B. Quon and R. Wuerker, Proc. 2nd Workshop on Hot Electron Ring Physics, N. A. Uckan, ed., Conf-811203 (June 1982) p. 519.

8. T. K. Samec, B. I. Hauss and G. Guest, Proc. 2nd Workshop on Hot Electron Ring Physics, N. A. Uckan, ed. Conf-811203 (June 1982) p. 531.

9. T. D. Rognlien, Nuclear Fusion 23,163 (1983).

10. J. E. Howard, A. J. Lichtenberg and M. A. Lieberman, Physica 5D,243 (1982).

11. J. E. Howard, M. A. Lieberman, A. J. Lichtenberg and R. H. Cohen, in Proc. 2nd Workshop on Hot Electron Ring Physics, N. A. Uckan, ed., Conf-811203 (June 1982) p. 561.

12. A. J. Lichtenberg and M. A. Lieberman, Regular and Stochastic Motion, Springer-Verlag, 1983.

13. M. Seidl, Plasma Phys. 6,597 (1964).

14. R. S. McKay, "Renormalization in Area Preserving Maps," Ph.D. Thesis, Princeton University (1982).

15. J. E. Howard and S. M. Hohs, "Stochasticity and Reconnection in Hamiltonian Systems," to be published in Phys. Rev. A.

16. R. H. Cohen, in *Intrinsic Stochasticity in Plasmas,* A. Laval and D. Gresillon, ed., (1979) p. 181.

17. B. V. Chirikov, Sov. J. Plasma Phys. 4,289 (1979).

18. R. H. Cohen and G. Rowlands, Phys. Fluids 24,2295 (1981).

19. I. B. Bernstein and D. B. Baxter, Phys. Fluids 24, 108 (1981).

Table 1

Parameters for Two Experiments

STM: L = 20 cm, $\mathcal{E}$ = 10 V/cm, f = 10 GHz, $R_1 = 2$

MFTFB: L = 100 cm, $\mathcal{E}$ = 100 V/cm, f = 28 GHz, $R_1 = 2$

	M	$\Delta\omega/\omega$	σ	P_B	$E_{\perp B}(keV)$
STM	2200	.02	1/12	190	9.4
MFTF-B	5000	.016	1/16	355	650

FIGURE CAPTIONS

Fig. 1 Schematic of trapped electron orbit in a parabolic well, showing resonance zones corresponding to two heating frequencies.

Fig. 2 Fixed points in scaled action space.

Fig. 3 Projection of four-dimensional phase space onto $I-\phi$ plane for M = 500, σ = 0.25 and ϵ = 0.05, produced by scanning along the ϕ=45° line. True fixed points are indicated for n = 1, 2 and 3; the s-fold and r-fold fixed points exist strictly speaking in the limits $\epsilon \rightarrow 0$ and ∞, respectively.

Fig. 4 $I-\phi$ projection for the same conditions as in Fig. 3 except that ϵ=1. The n = 1 fixed point has destabilized, in accord with the predictions of Section III.

Fig. 5 Stability of fixed points in $\phi-\chi$ plane for large M and small ϵ with (a) J = 0; (b) J $\neq$ 0.

Fig. 6 Calculated stability boundaries in $\epsilon - M$ plane for J = 0. The eigenvalue configurations are shown in the inserts.

Fig. 7 Numerically obtained stability boundaries in $\epsilon - M$ plane for J $\neq$ 0.

Fig. 8 Resonance curves in action space for M = 500 and σ = 0.25. Intersections of n_r and n_s resonances correspond to the fixed points of Fig. 2.

Fig. 9 Calculated resonance widths for the n_s resonances ($\epsilon \rightarrow 0$) for M = 500 and σ = 0.25.

Fig. 10 Calculated resonance widths for the n_r resonances ($\epsilon \rightarrow \infty$) for M = 500 and σ = 0.25.

Fig. 11 Adiabatic barrier in action space determined from a number of orbits initialized near the I = J line in the stochastic sea. Parameters are as in Figs. 9 and 10 except that ϵ = 1.0. The theoretical resonance widths of Figs. 9 and 10 are superposed.

Fig. 12 Computed thick-layer diffusion coefficients compared with theoretical quasilinear values for M = 20000, σ = 0.25, ϵ = 0.8 and initial values for I_0 = 10, J_0 = 20.

Fig. 13 Computed thin-layer diffusion coefficient for M = 240, σ = 0.25, ϵ = 3.0.

Fig. 14 Sketch showing boundary conditions used in axial loss model.

Fig. 15 Enlargement of computed adiabatic barrier for same conditions as Fig. 11, used in finding the shape of the stochastic region for the axial loss calculation.

Fig. 16 Average loss energy J_L and loss time τ_L from axial loss model (curves) compared with numerical values (circles).

Fig. 17 Stability diagram for general fourth order symplectic matrix (after MacKay). Corresponding eigenvalue configurations are shown as inserts. Only the inner arrowhead is stable.

Fig. 18 Root locus for m = 0, n = 1, fixed point, with M = 50, σ = 0.25, and $\phi = \pi/4, \chi = 3\pi/4$. A Krein collision occurs when ϵ = 4/9.

Fig. 19 Geometry of s-fold resonance curve. The extremum occurs on the line P = 5 σ J/2 at the velocity $u^* = 2u_0/3$.

Fig. 20 Integrable representation of Hamiltonian level curves for motion near an extremum of the resonance curve of Fig. 19. Reconnection occurs when $H_1 = H_2$.

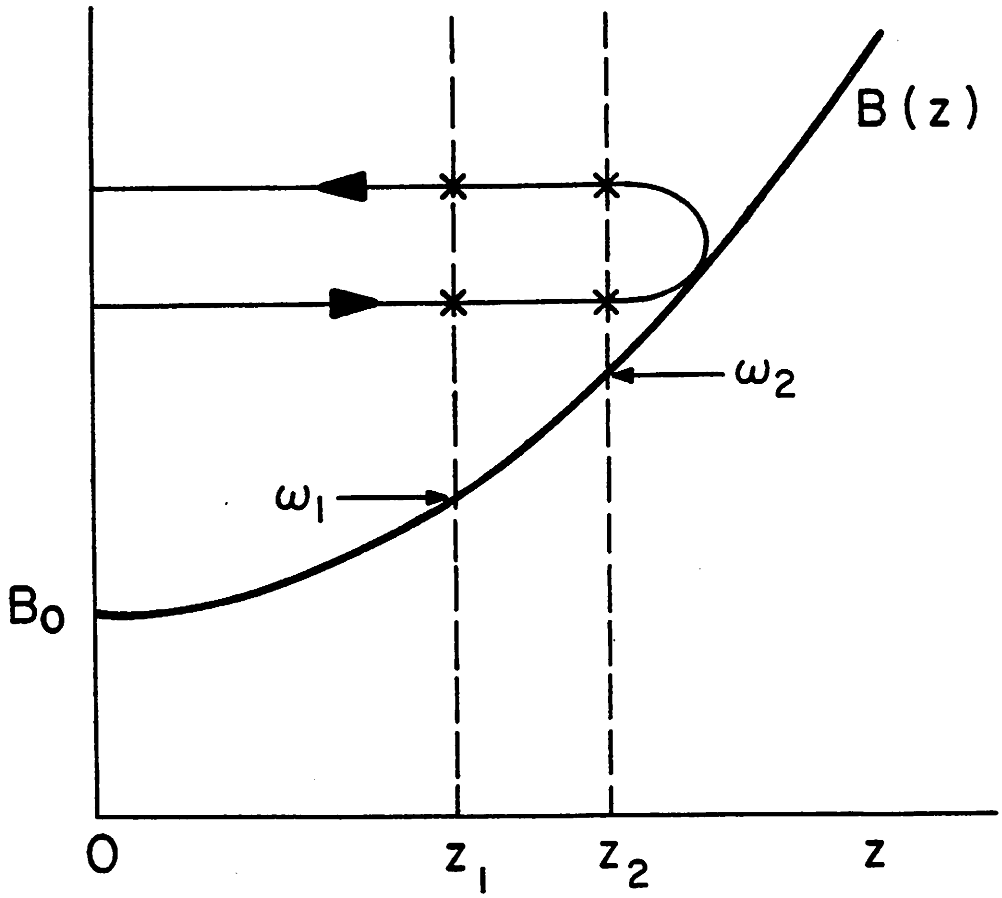

B(z)
ω2
ω1
Bo
O
z1
z2
z

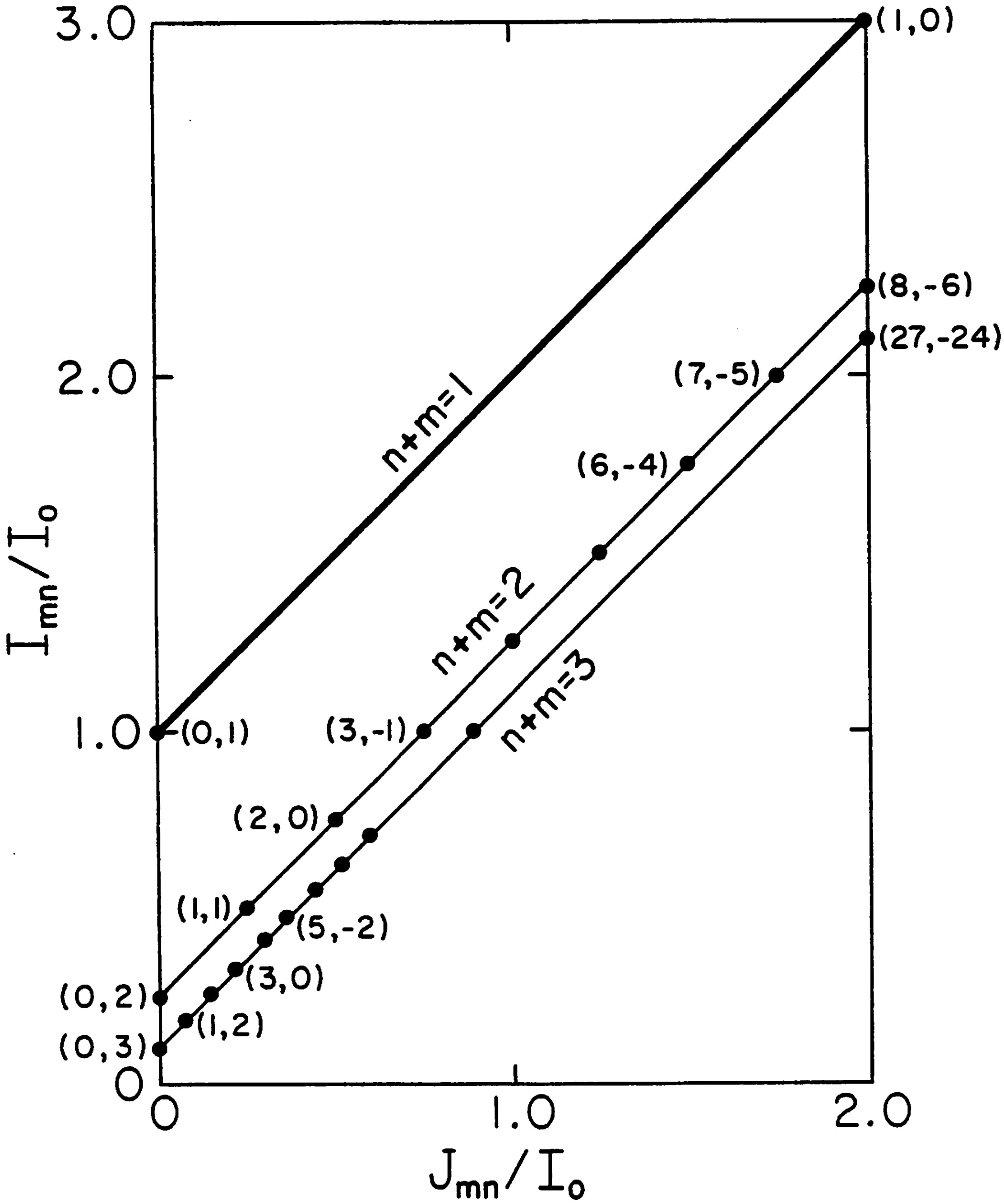

3.0
2.0
1.0
0
0
1.0
2.0
I_{mn}/I_o
J_{mn}/I_o
n+m=1
n+m=2
n+m=3
(1,0)
(8,-6)
(27,-24)
(7,-5)
(6,-4)
(3,-1)
(2,0)
(1,1)
(5,-2)
(3,0)
(0,1)
(0,2)
(1,2)
(0,3)

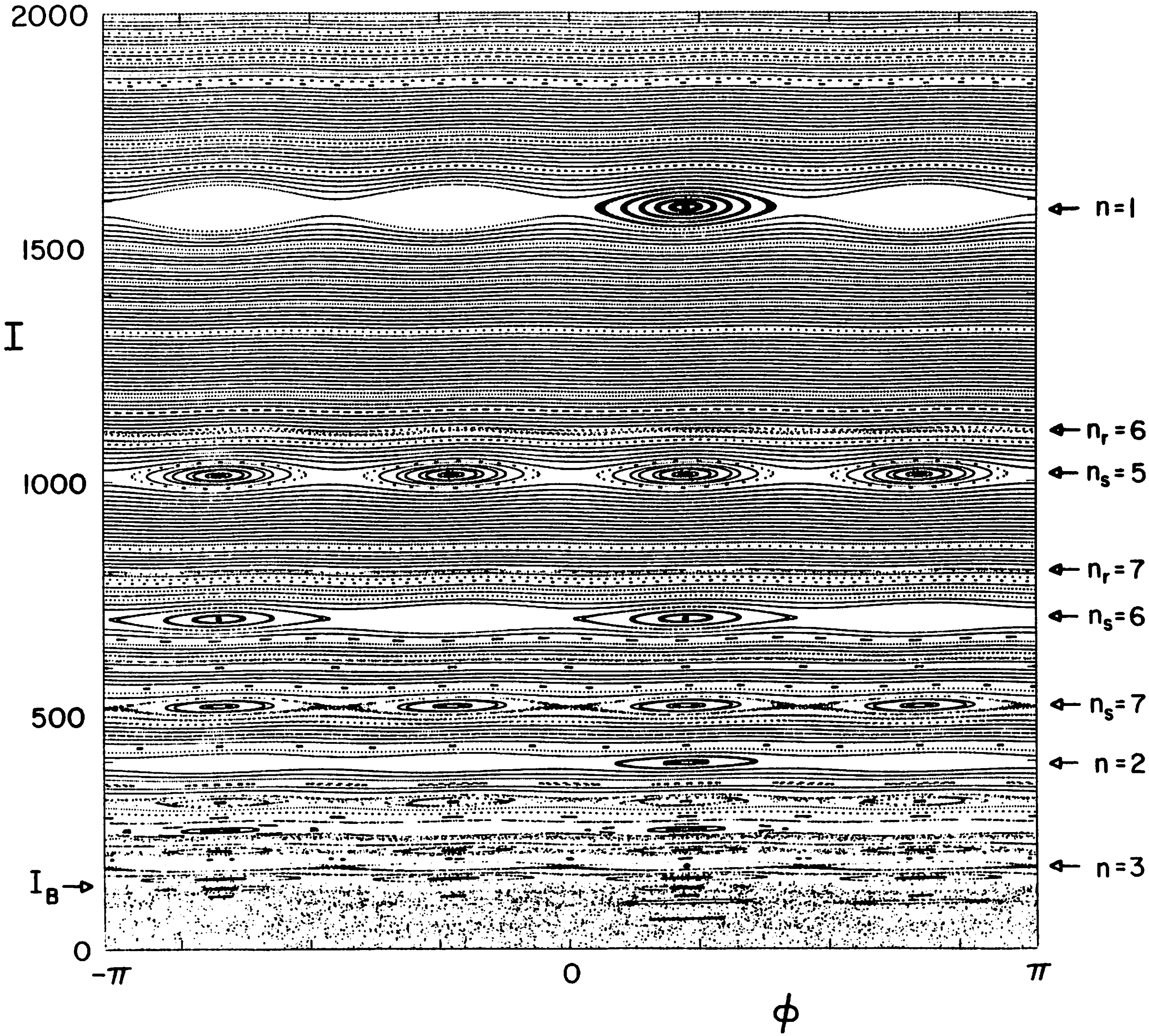

2000
1500
1000
500
0
I
I_B
$-\pi$
0
π
ϕ
n=1
$n_r=6$
$n_s=5$
$n_r=7$
$n_s=6$
$n_s=7$
n=2
n=3

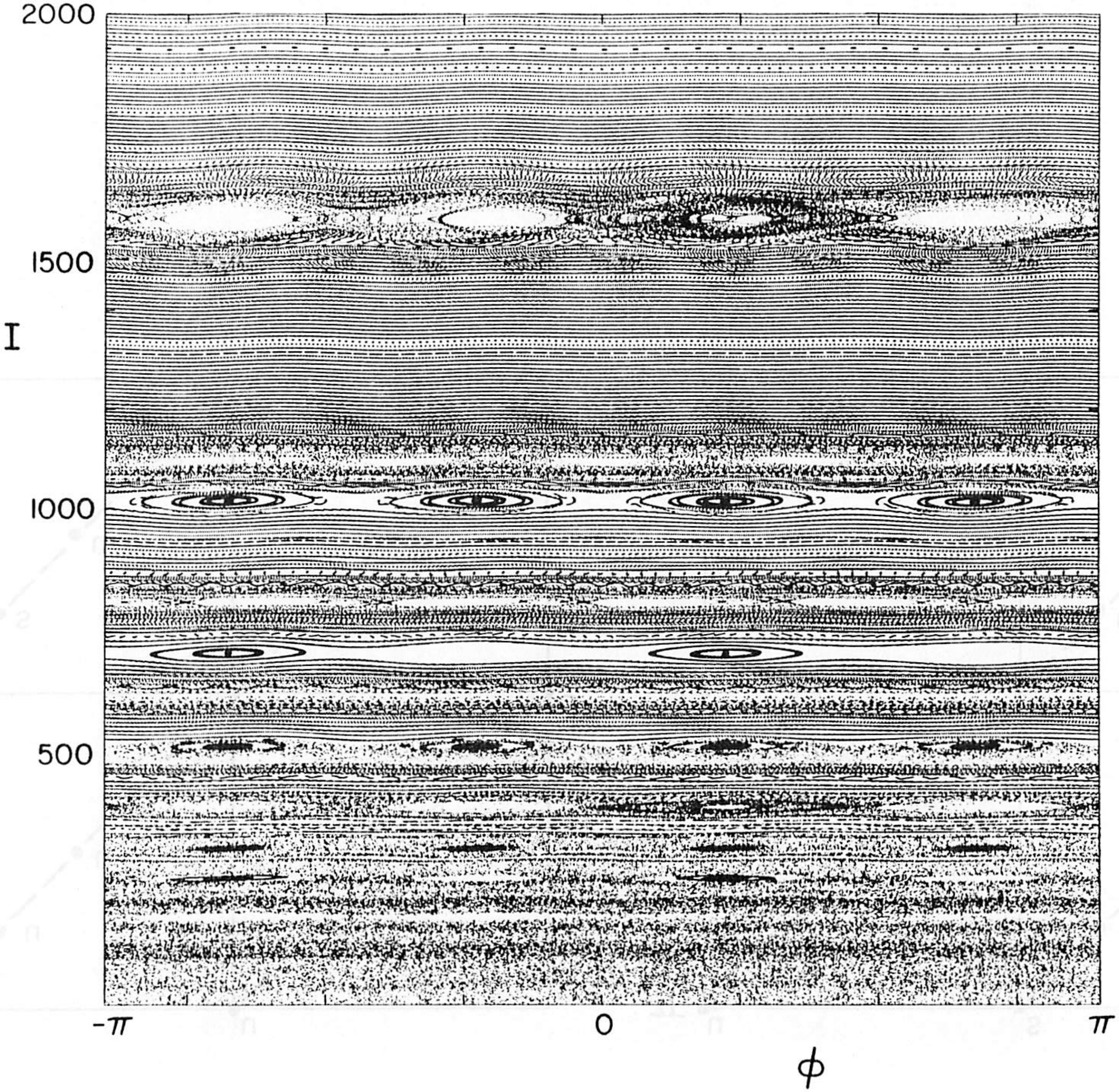
2000
1500
I
1000
500
-π
0
π
ϕ

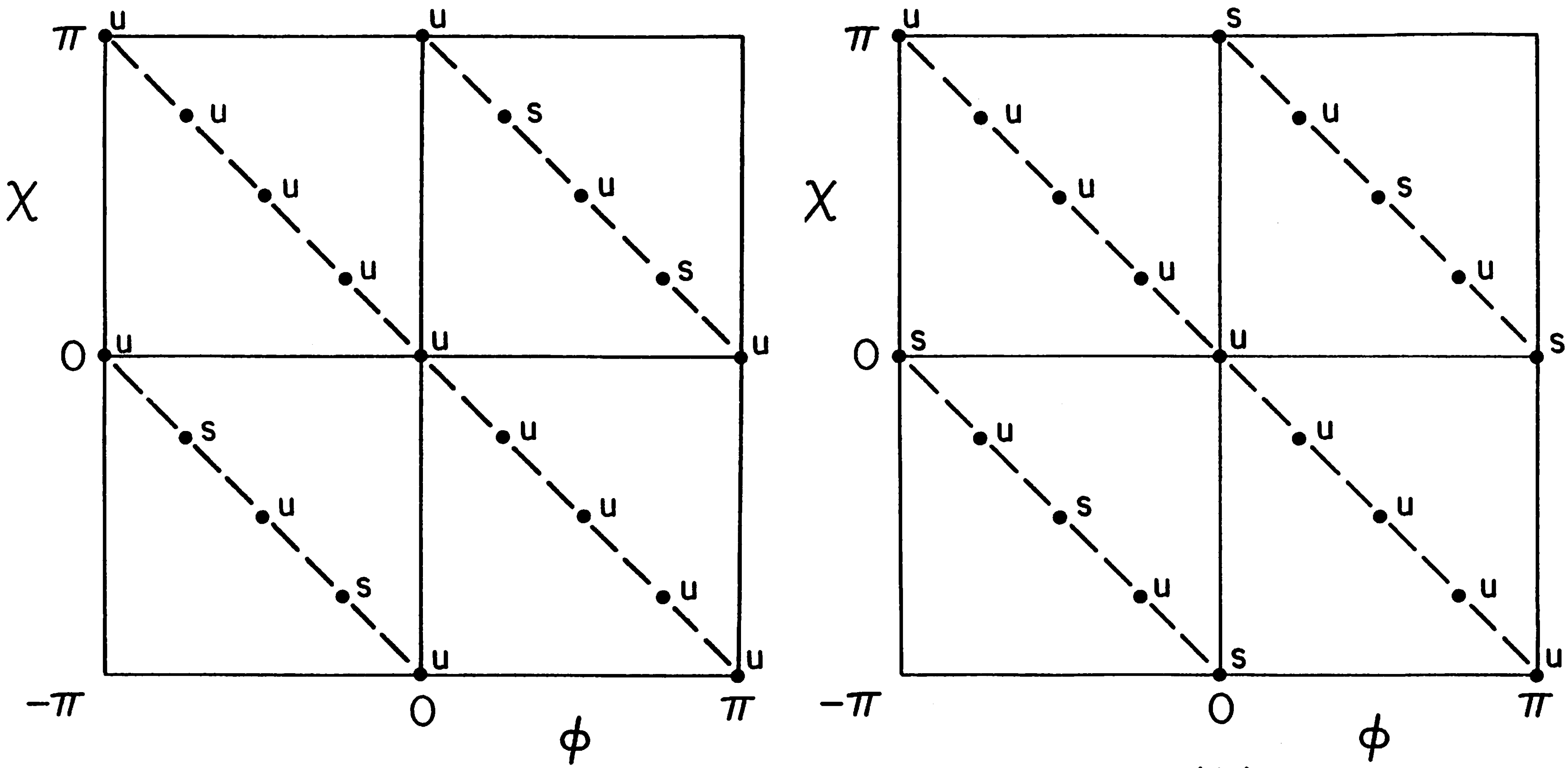

(a)

(b)

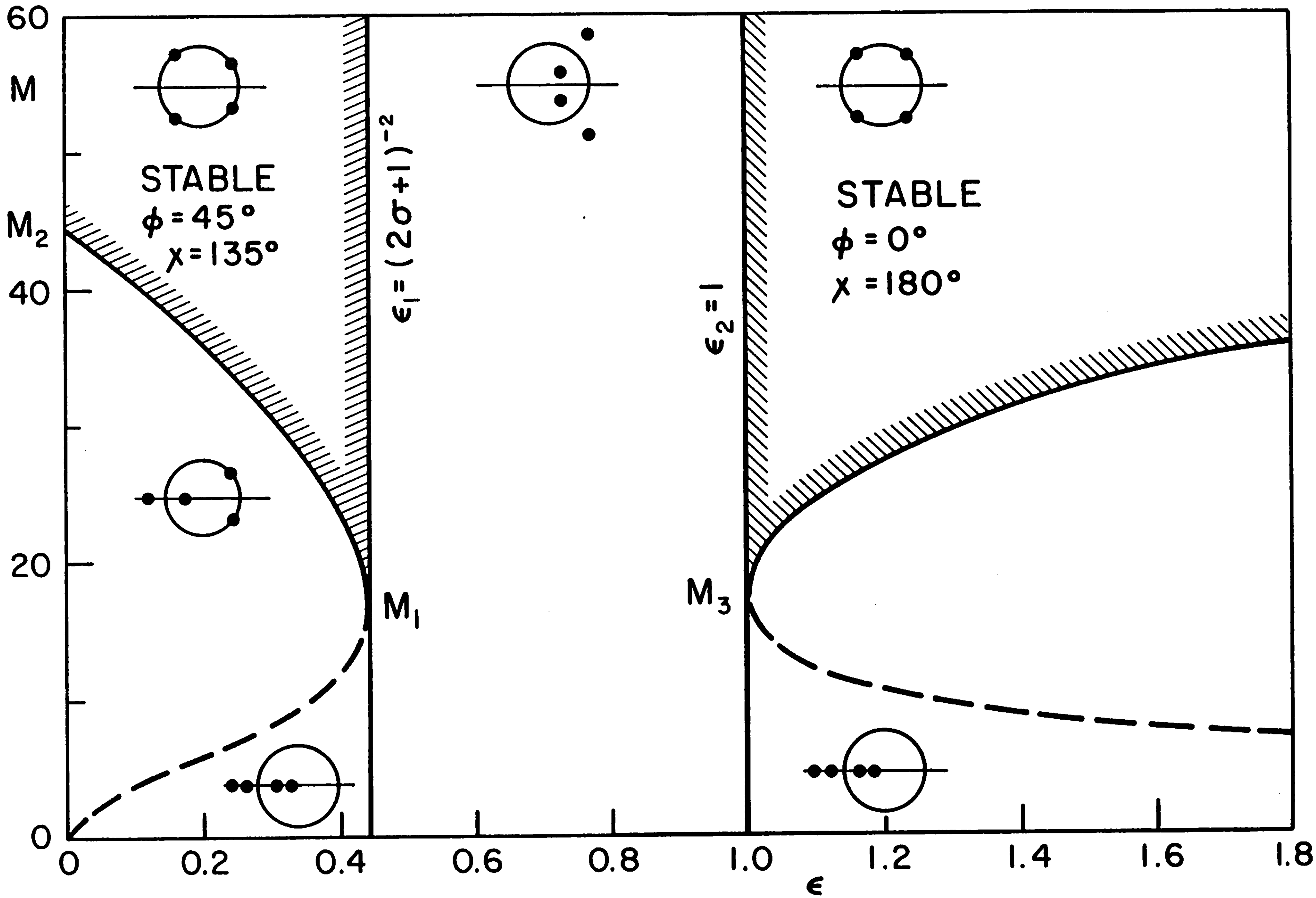

60
40
20
0
M
M_2
M_1
M_3
STABLE
$\phi = 45°$
$\chi = 135°$
$\epsilon_1 = (2\sigma+1)^{-2}$
$\epsilon_2 = 1$
STABLE
$\phi = 0°$
$\chi = 180°$
0
0.2
0.4
0.6
0.8
1.0
1.2
1.4
1.6
1.8
ϵ

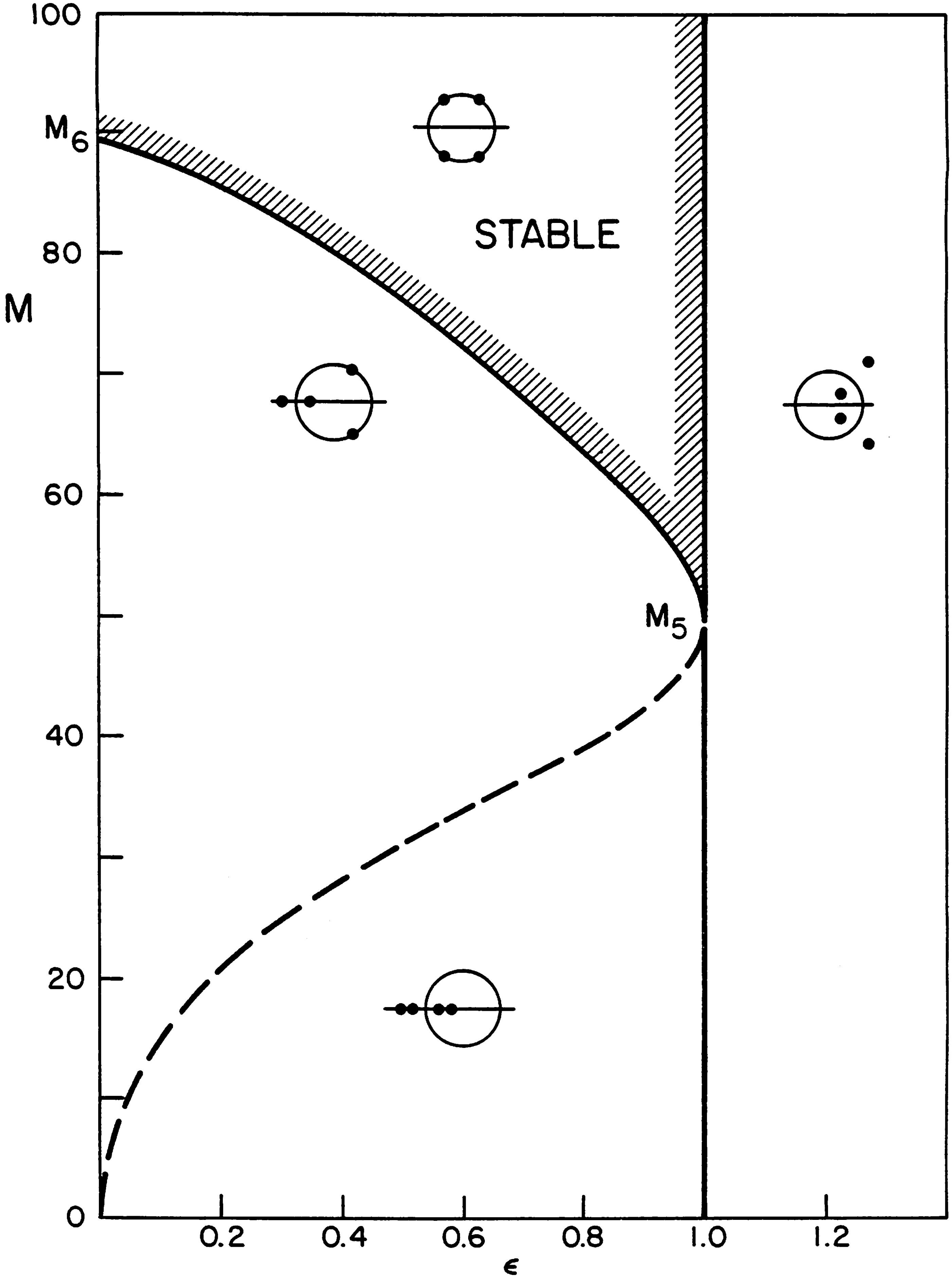

100
80
60
40
20
0
M
M_6
M_5
STABLE
0.2
0.4
0.6
0.8
1.0
1.2
ε

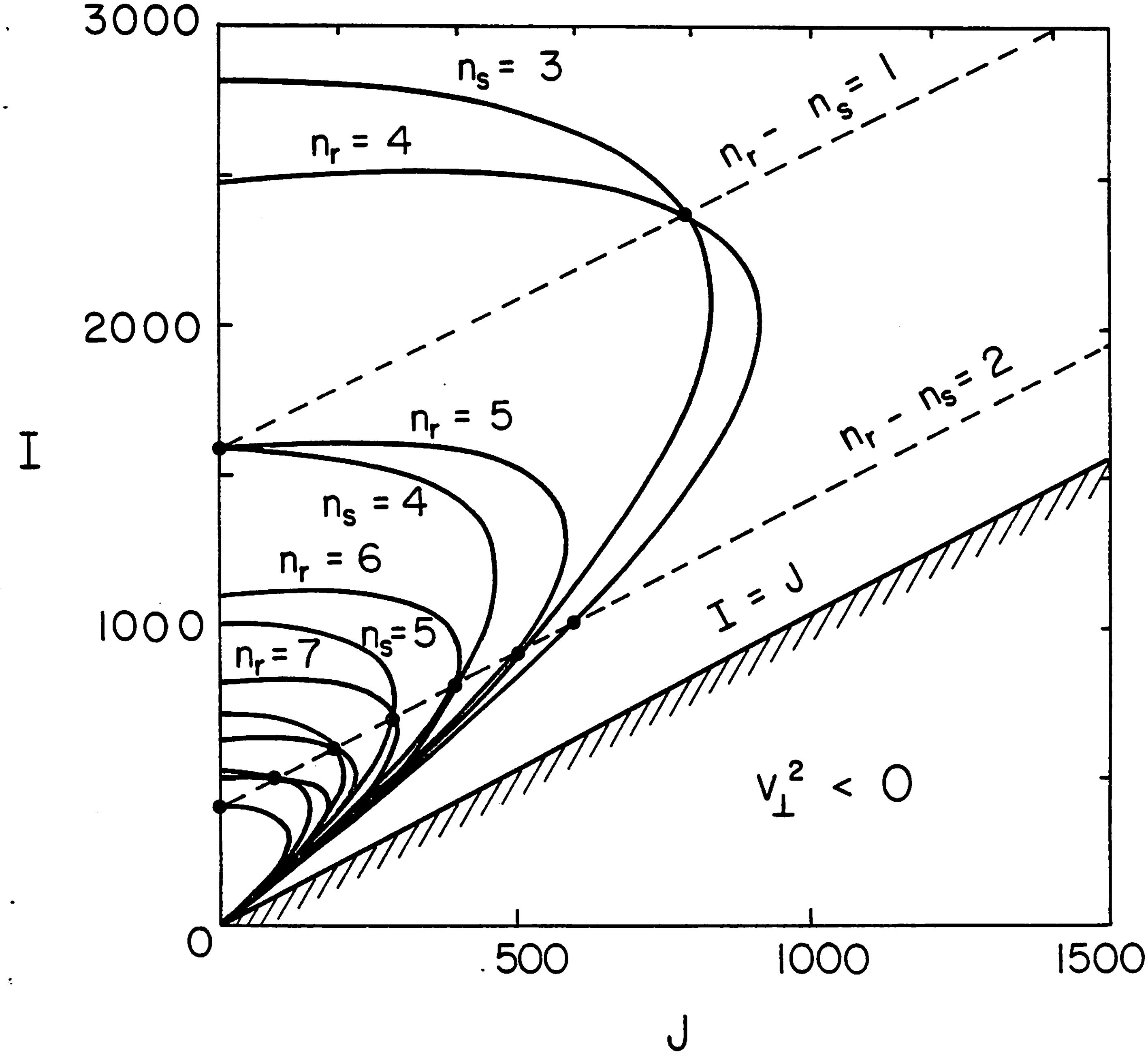
3000
2000
1000
0
500
1000
1500
I
J
$n_s = 3$
$n_r = 4$
$n_r - n_s = 1$
$n_r = 5$
$n_s = 4$
$n_r = 6$
$n_s = 5$
$n_r = 7$
$n_r - n_s = 2$
$I = J$
$V_\perp^2 < 0$

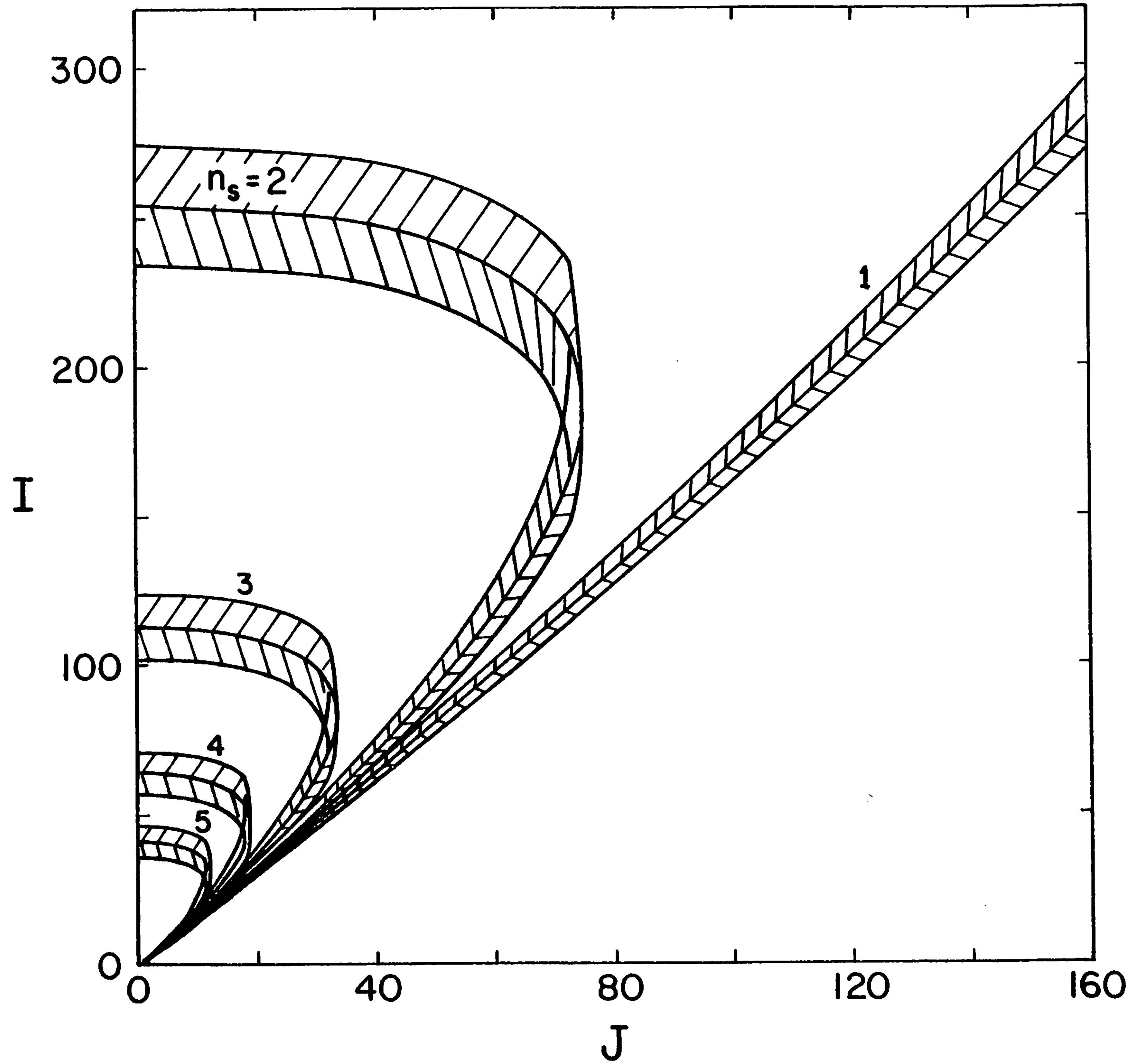

300
200
100
0
I
0
40
80
120
160
J
$n_s = 2$
3
4
5
1

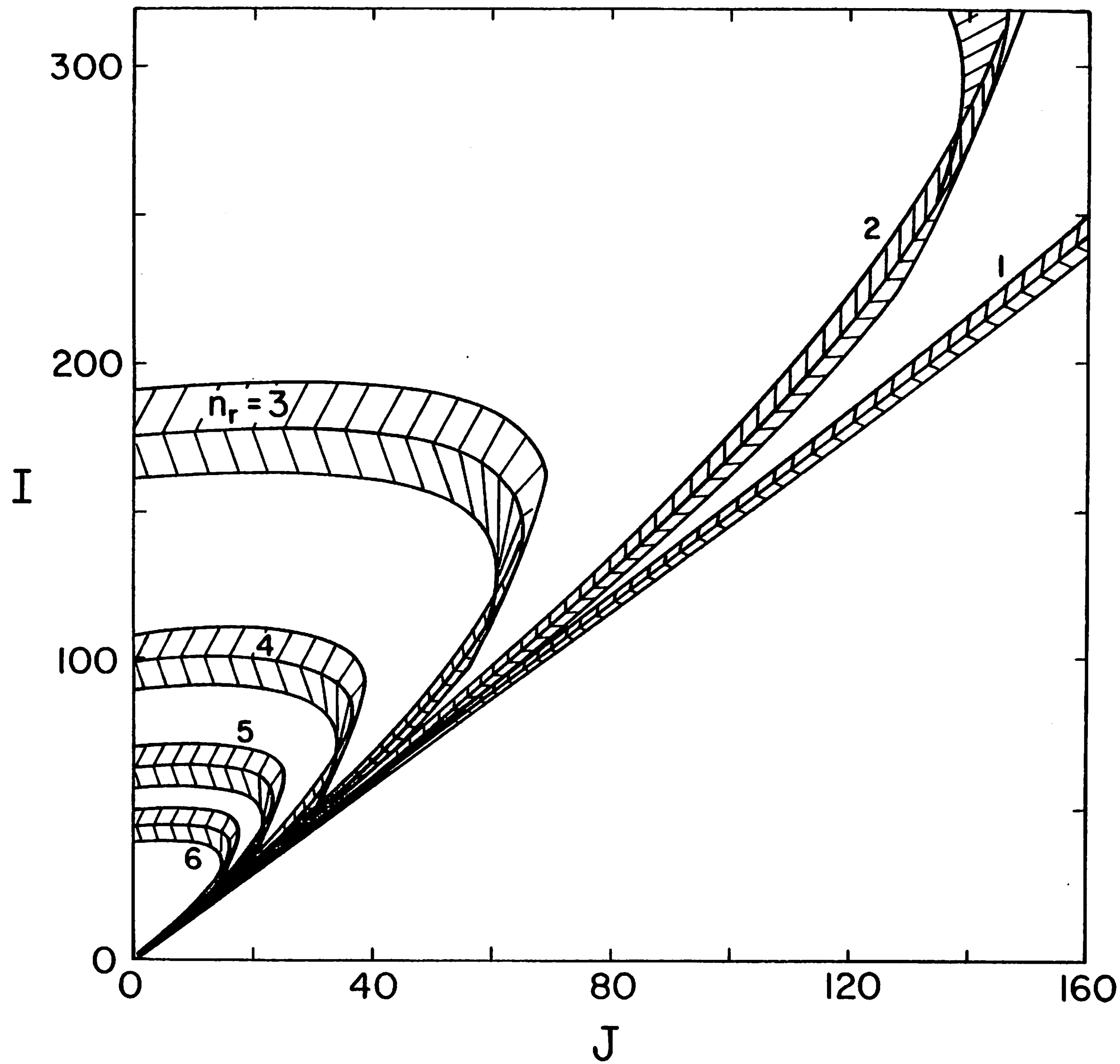

300
200
100
0
I
0
40
80
120
160
J
n_r = 3
2
1
4
5
6

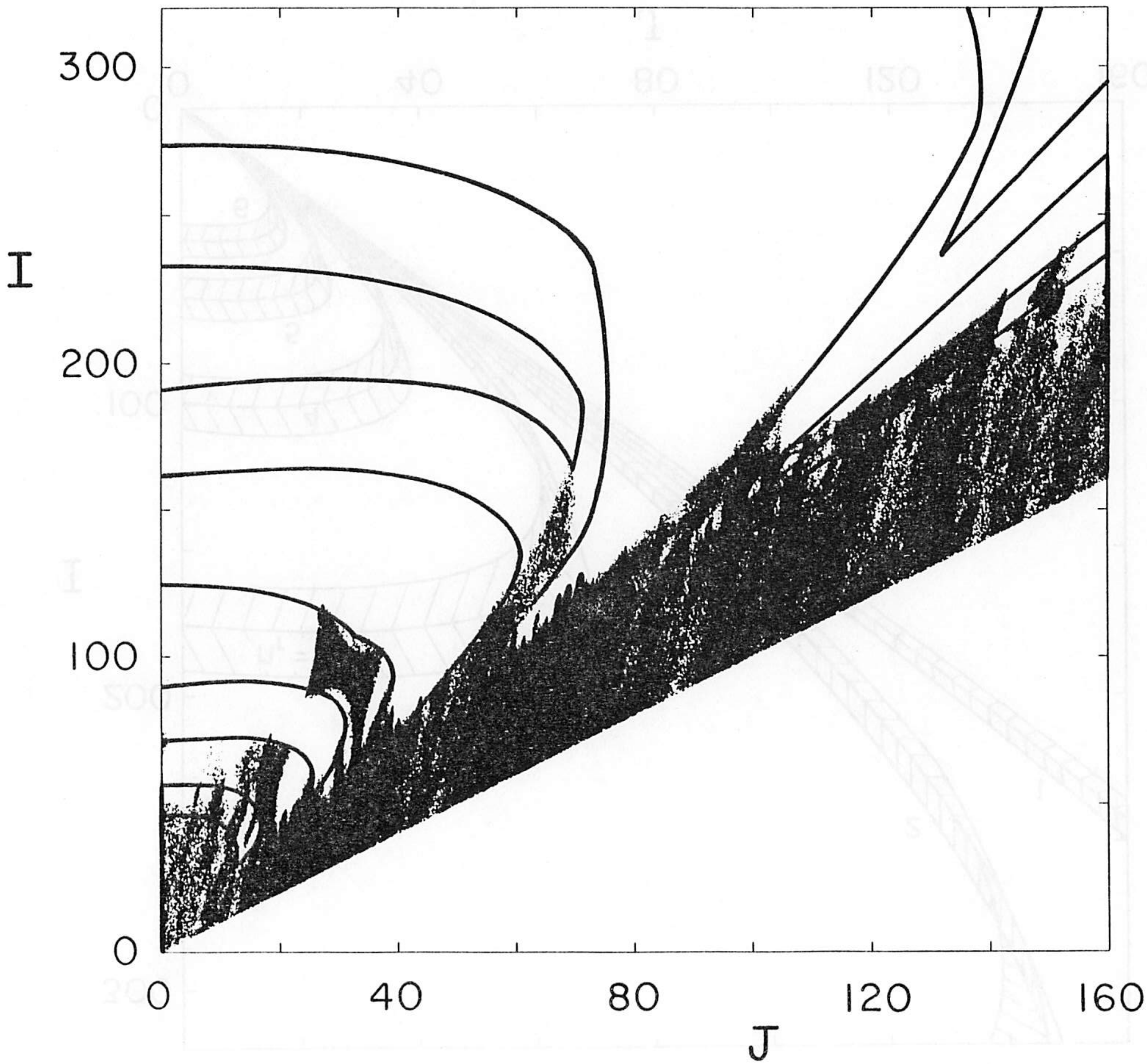

300
200
100
0
I
0
40
80
120
160
J

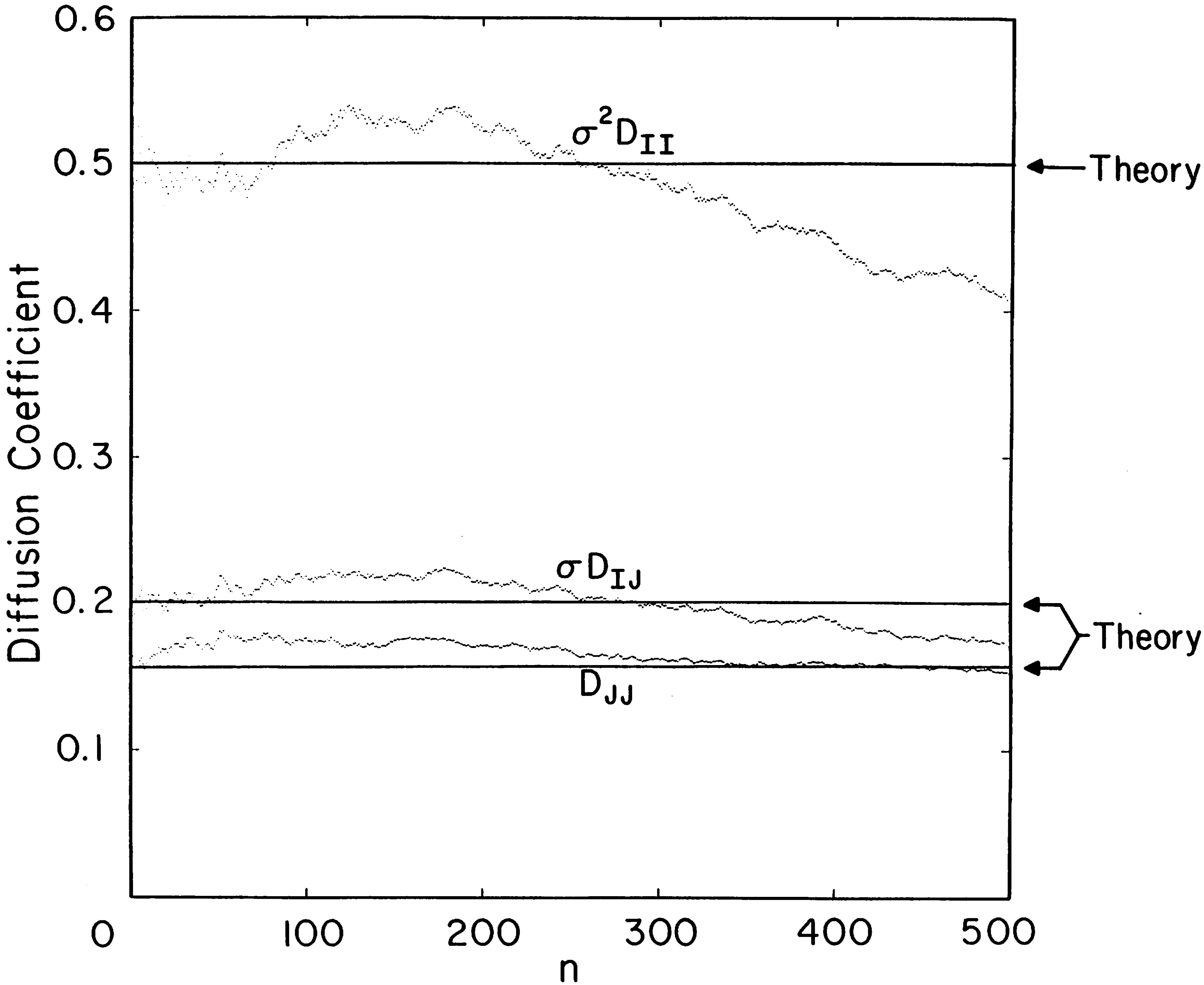

0.6
0.5
0.4
0.3
0.2
0.1
0
100
200
300
400
500
n
Diffusion Coefficient
$\sigma^2 D_{II}$
σD_{IJ}
D_{JJ}
Theory
Theory

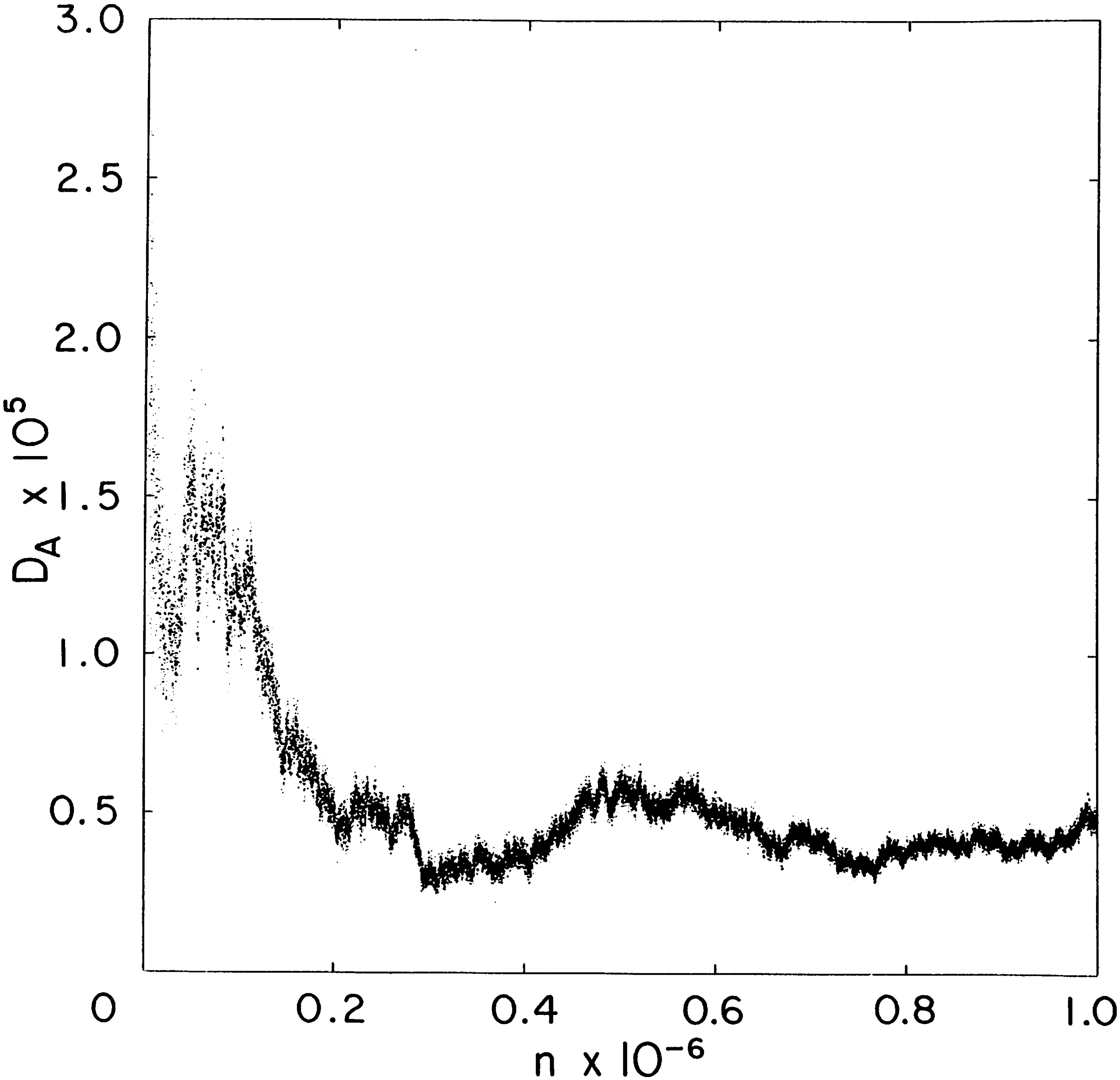
3.0
2.5
2.0
1.5
1.0
0.5
$D_A \times 10^5$
0
0.2
0.4
0.6
0.8
1.0
$n \times 10^{-6}$

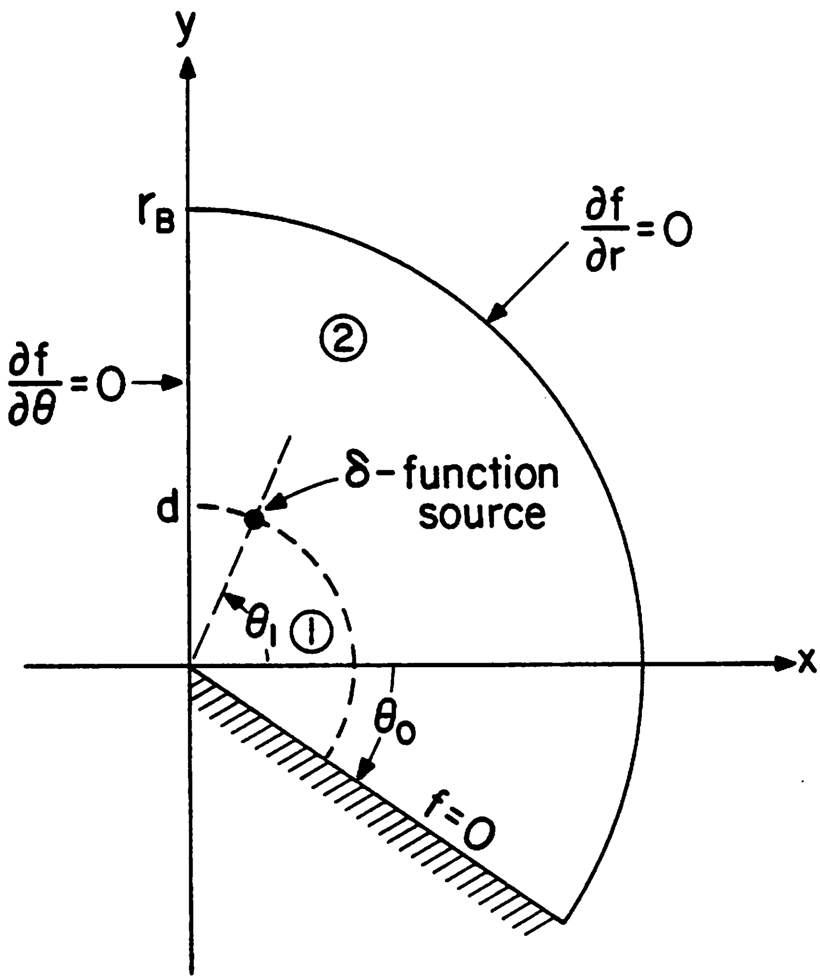
y
r_B
$\frac{\partial f}{\partial r} = 0$
②
$\frac{\partial f}{\partial \theta} = 0$
δ-function
source
d
θ_1
①
x
θ_0
f=0

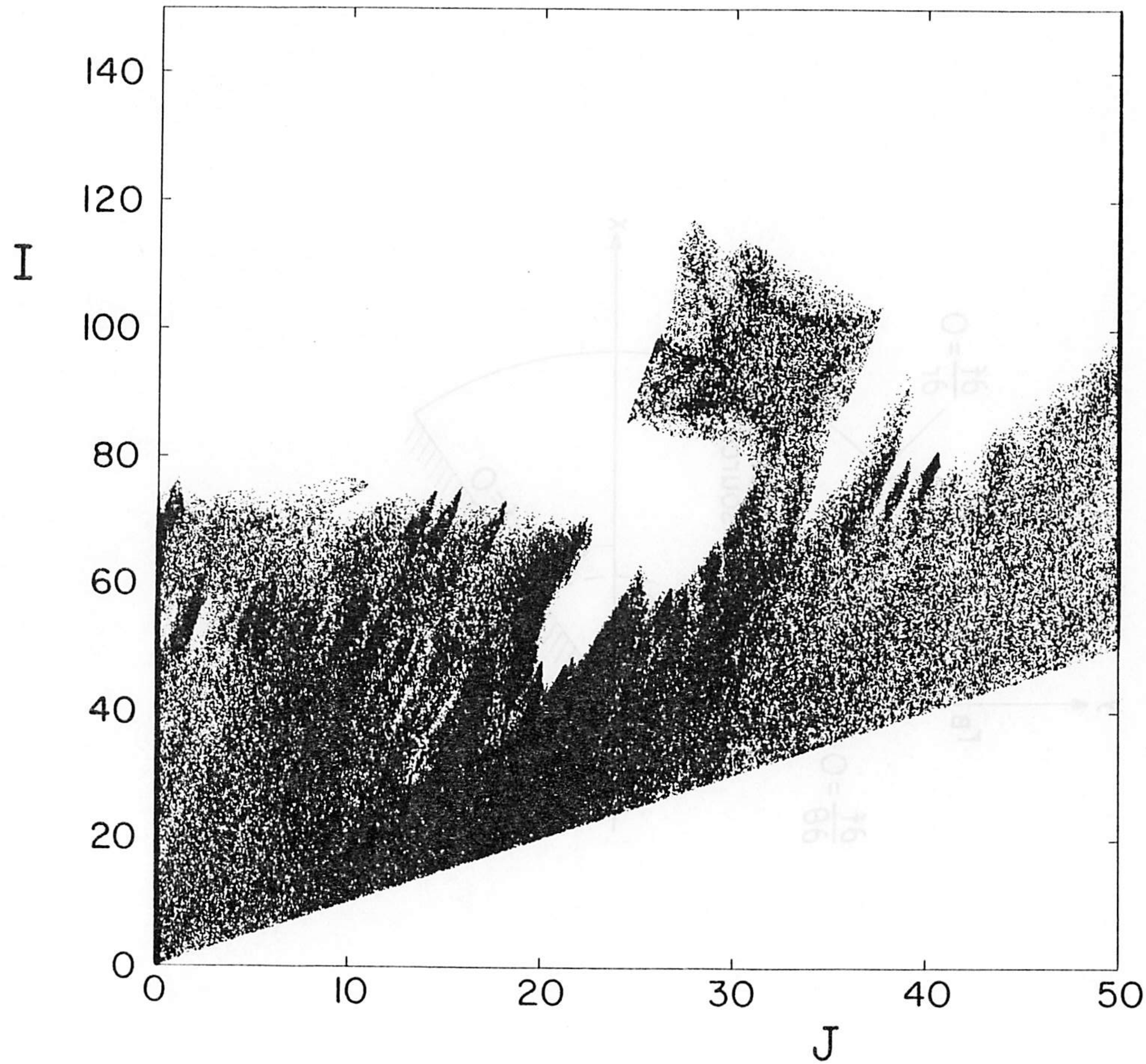

140
120
I
100
80
60
40
20
0
0
10
20
30
40
50
J

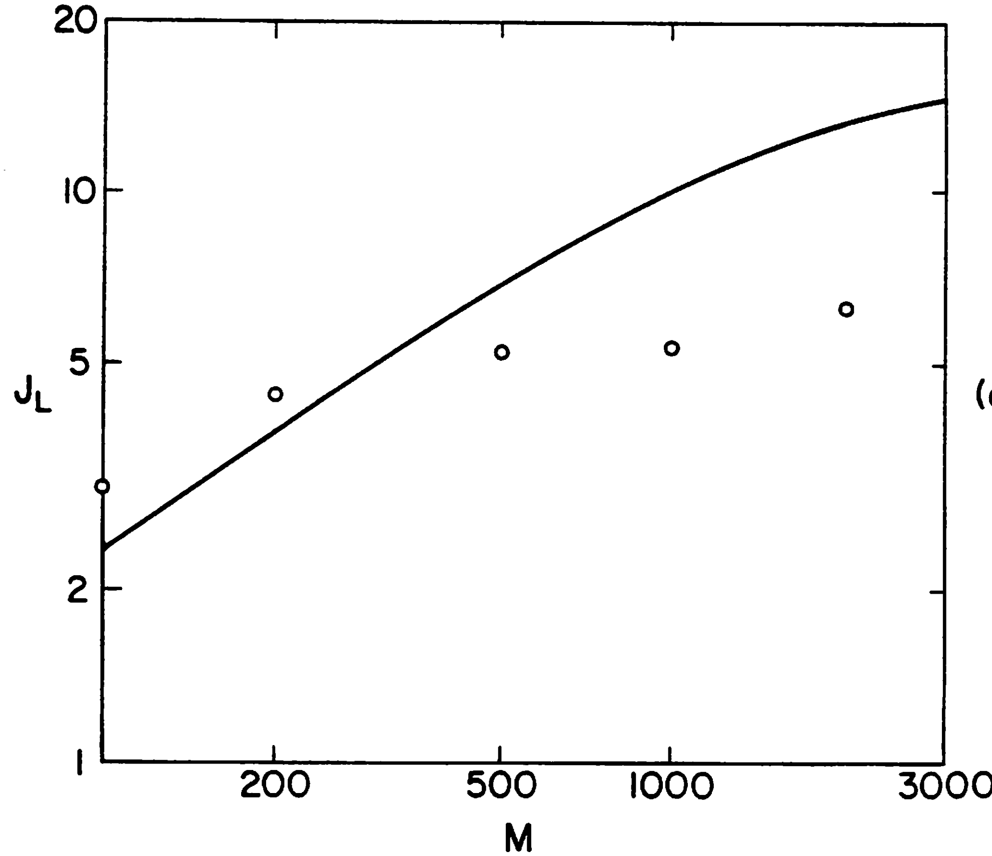

20
10
5
2
1
J_L
200
500
1000
3000
M

(a)

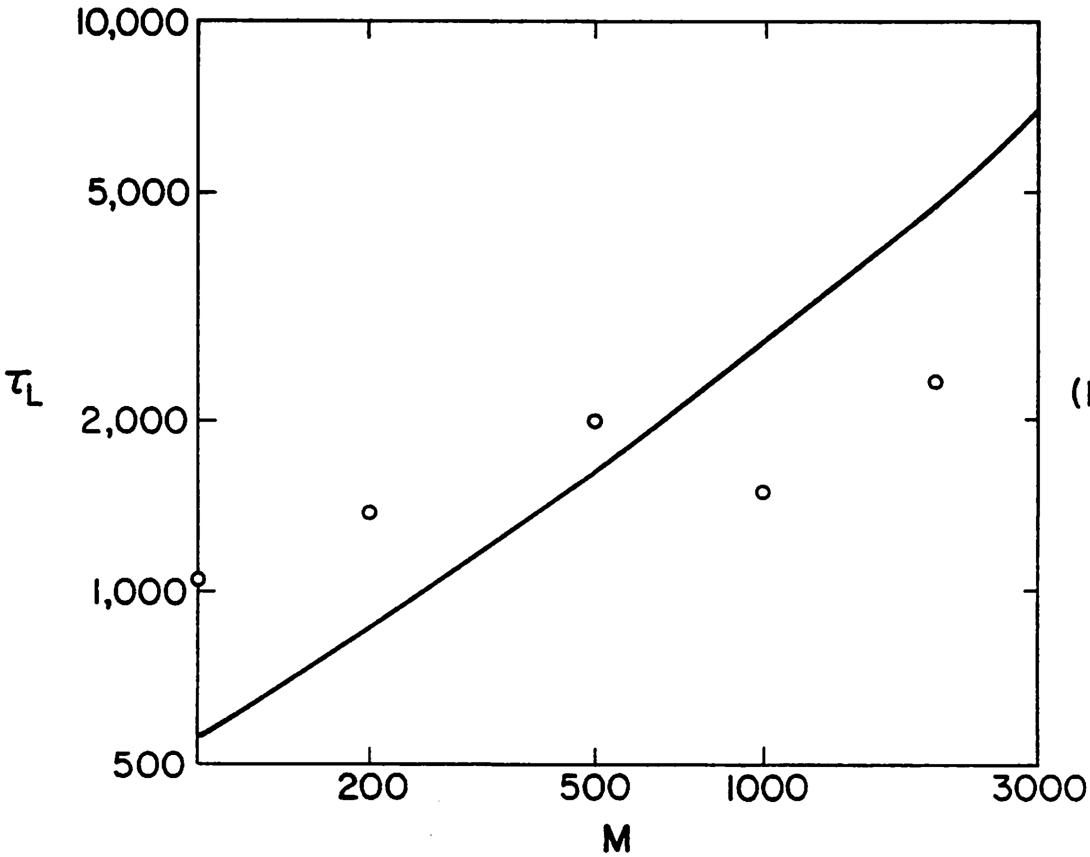

10,000
5,000
2,000
1,000
500
τ_L
200
500
1000
3000
M

(b)

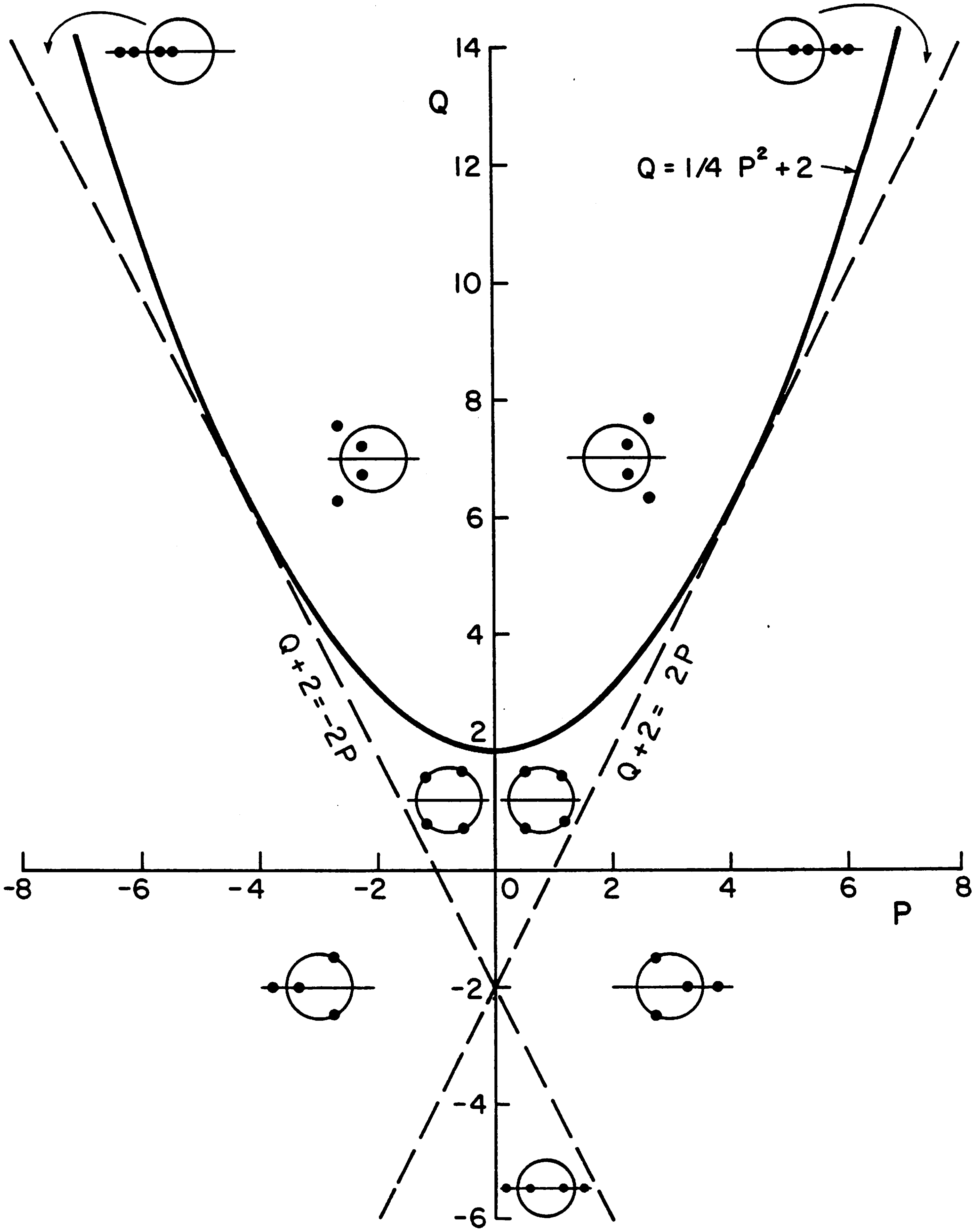

Q
14
12
10
8
6
4
2
-2
-4
-6
Q = 1/4 P² + 2
Q + 2 = -2P
Q + 2 = 2P
-8
-6
-4
-2
0
2
4
6
8
P

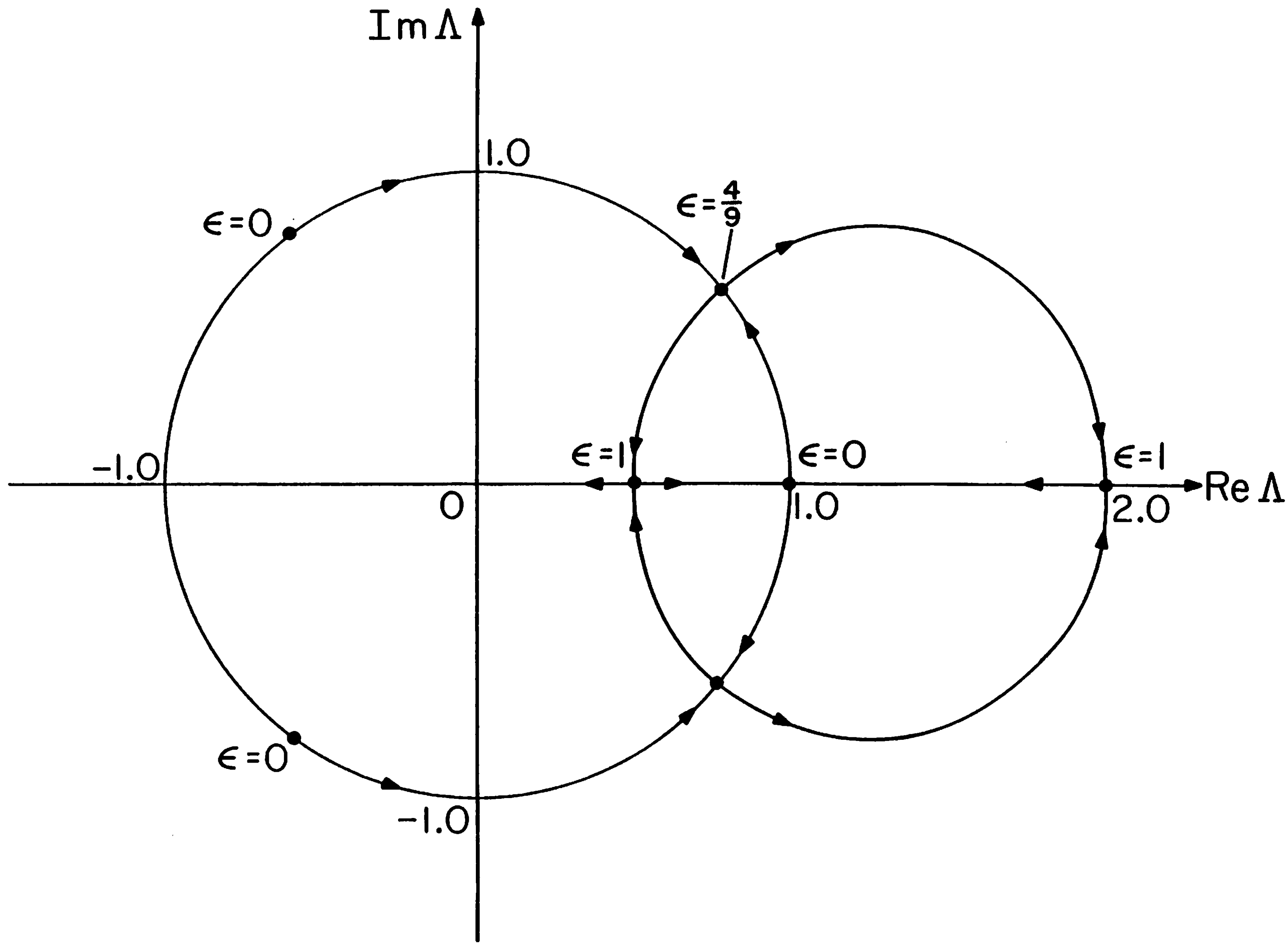
Im Λ
1.0
ε=0
ε=4/9
-1.0
ε=1
ε=0
ε=1
Re Λ
0
1.0
2.0
ε=0
-1.0

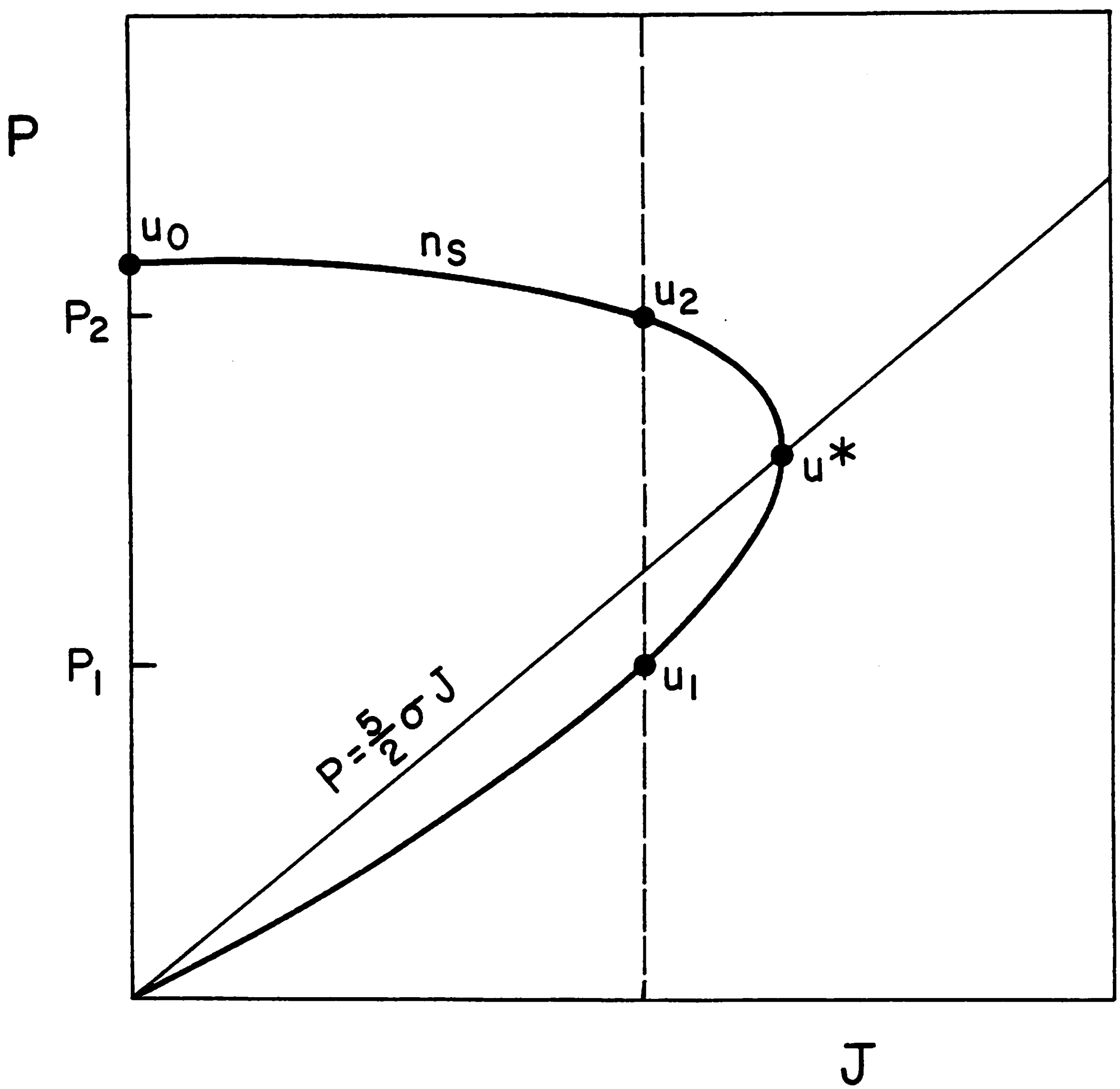

P
u_0
n_s
u_2
P_2
u^*
P_1
u_1
$P = \frac{5}{2}\sigma J$
J

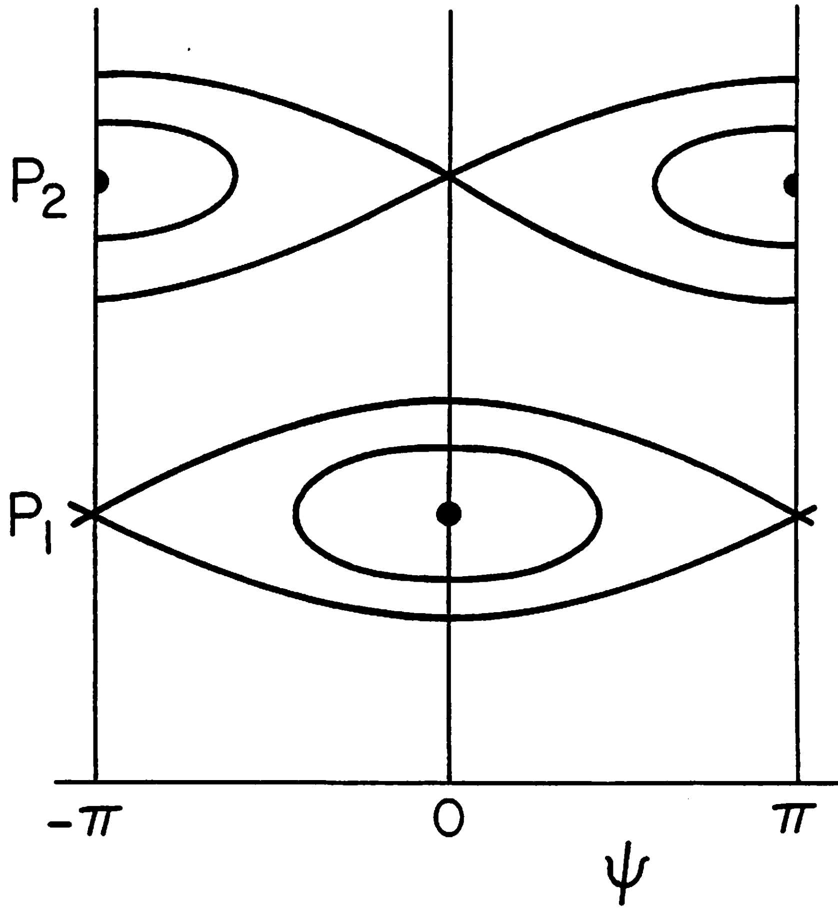

(a)

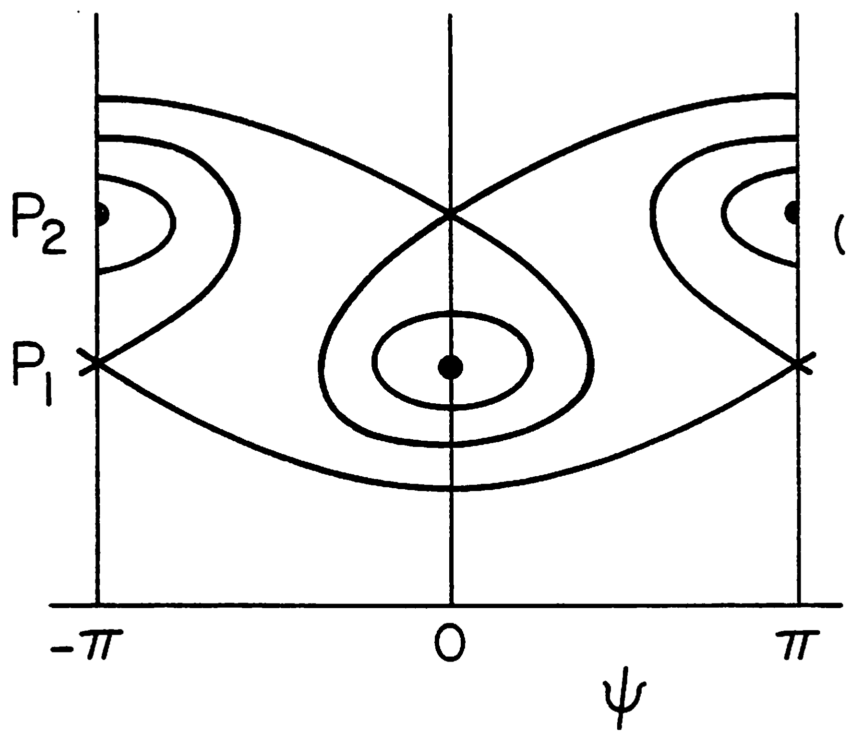

(b)